

See discussions, stats, and author profiles for this publication at: <https://www.researchgate.net/publication/281664588>

# Entry Trajectory Optimization by Second-Order Cone Programming

**Article** in *Journal of Guidance Control and Dynamics* · August 2015

DOI: 10.2514/1.G001210

CITATIONS

32

READS

419

## 3 authors:



**Xinfu Liu**

Beijing Institute of Technology

**10** PUBLICATIONS **203** CITATIONS

SEE PROFILE



**Zuojun Shen**

Beihang University (BUAA)

**5** PUBLICATIONS **65** CITATIONS

SEE PROFILE



**Ping Lu**

San Diego State University

**118** PUBLICATIONS **2,533** CITATIONS

SEE PROFILE

## Some of the authors of this publication are also working on these related projects:



Flight Dynamics and Control [View project](#)



trajectory optimization [View project](#)

# Entry Trajectory Optimization by Second-Order Cone Programming

Xinfu Liu<sup>\*</sup> and Zuojun Shen<sup>†</sup>

*Beihang University, Beijing 100191, China*

Ping Lu<sup>‡</sup>

*Iowa State University, Ames, Iowa 50011-2271*

Convex optimization has found wide applications in recent years due to its unique theoretical advantages and the polynomial-time complexity of state-of-the-art solution algorithms for convex programming. This paper represents an attempt to apply second-order cone programming, a branch of convex optimization, to the class of highly nonlinear trajectory optimization problems in entry flight. The foremost challenge in applying convex optimization in most aerospace engineering problems lies in the nonlinearity and non-convexity of the problem. Exclusive reliance on linearization does not always work well as is the case in entry trajectory optimization. This paper focuses on how to formulate realistic, highly constrained entry trajectory optimization problems in a fashion suitable to be solved by second-order cone programming with a combination of successive linearization and relaxation techniques. Rigorous analysis is conducted to support the soundness of the approach. Numerical demonstrations are provided to show the efficacy and effectiveness of the proposed method.

## I. Introduction

Convex optimization has gained increasing popularity in applications in aerospace guidance and trajectory planning in recent years. Sampled applications include planetary powered landing [1–5], spacecraft rendezvous and proximity operations [6–9], spacecraft trajectory optimization using differential drag [10], and spacecraft swarm flight [11]. Second-order cone programming (SOCP) – a subclass of convex optimization – where the cost function is linear, subject to linear equality and second-order cone constraints [12–14], has proved to be particularly appealing. An SOCP problem can be solved very efficiently and reliably by primal-dual interior-point methods (IPMs) [15–17] which have only polynomial complexity. That is, for any given accuracy, a solution is guaranteed to be found within a pre-determinable upper bound on the number of iterations which is a polynomial function of the problem dimensions, whenever a feasible solution exists. In practice, the typical number of iterations required for convergence tends to be much smaller than the theoretical bounds, and is almost independent of the problem dimensions [15–17]. In addition, a well designed primal-dual IPM does not require any user-supplied initial guesses, and it can provide a certificate when the problem is infeasible [18]. With all these benefits, practical application of SOCP has also been demonstrated in flight tests using customized IPMs onboard in real-time [19].

---

<sup>\*</sup>Postdoctoral Research Associate, School of Aeronautic Science and Engineering, lau.xinfu@gmail.com.

<sup>†</sup>Professor, School of Aeronautic Science and Engineering, shenzuojun@buaa.edu.cn

<sup>‡</sup>Professor, Department of Aerospace Engineering, plu@iastate.edu. Associate Fellow AIAA.

Most aerospace engineering problems, however, do not naturally have the specific form required in SOCP. Either the dynamics and the equality constraints are not linear, or the inequality constraints are not second-order cones, or even convex. Considerable efforts are required to carefully cast an original problem into the framework of SOCP. This process involves creative re-formulation and thorough analysis to establish that the SOCP solution is the solution of the original problem. This is the essence of the lossless convexification techniques and theory developed for the powered landing problem in Refs. [1–5], and relaxation methodology for the problem of spacecraft rendezvous and proximity operations in Refs. [6, 7, 9]. Other techniques involving change of variables and making use of physical insights have also been adopted for robotic problems [20, 21]. These convexification and relaxation procedures are problem-dependent, and their designs determine whether the original problem can be successfully solved by using SOCP.

Despite the upfront investment in time and effort required in tailoring a practical problem to be suitable for the SOCP-based methodology, the payoff can be significant because of the aforementioned advantages of SOCP. This paper further expands the list of aerospace engineering problems that can be solved by the modern tool of SOCP. Specifically, the focus here is on the class of problems of entry/hypersonic gliding trajectory planning and optimization, subject to all common constraints in terminal condition, heating and load path constraints, and (possibly multiple) no-fly zones (NFZs). The problems of entry/gliding trajectory optimization have been investigated broadly in the literature. The pseudospectral optimal control approach is widely used to solve various trajectory optimization problems in entry and hypersonic gliding flight [22–26]. A fast optimization approach is presented in Ref. [27] where the trajectory is parameterized by simple basis functions and the solution is obtained by a nonlinear programming method. In the spirit of the Space Shuttle entry guidance design [28], a reference profile for the entry trajectory is obtained by optimizing the drag profile as a nonlinear constrained optimization problem [29]. A Shuttle entry trajectory optimization problem is also solved in Ref. [30] to demonstrate collocation and mesh-refinement techniques.

At the core of the numerical process, most of the existing work solves the problem of entry trajectory optimization as a nonlinear programming problem (NLP) by a sequential quadratic programming method. This paper explores the use of the SOCP formulation and a primal-dual IPM to take the advantage of the unique properties of SOCP and state-of-the-art primal-dual interior-point algorithms developed over the last decade or so. Compared to other approaches, the use of SOCP in aerospace trajectory optimization is still in the early stage. Much still needs to be learned on how to make it work. The objective of this paper is not to replace the existing NLP-based approaches in entry trajectory optimization, but to expand the toolbox with an appealing new addition.

This paper formalizes a procedure and describes the detailed formulation of the entry trajectory optimization problem as a sequence of problems suitable to be solved by SOCP. In doing so, the very first obstacle is the nonlinearity in the system dynamics. The SOCP approach requires the state equations to be linear (in both state and control). Because of the presence of the aerodynamic forces, the entry flight problem has completely nonlinear dynamics, in contrast to the largely linear dynamics in space flight problems in Refs. [1–9, 11]. Sequential linearization is the usual technique to handle general nonlinearity [11, 31]. For the entry problem, it is discovered that sequential linearization of the system dynamics with respect to the control tends to cause significant undesired jitters in control profile, and convergence difficulty. A major part of this paper

is devoted to circumvent this difficulty. The technique developed in this paper consists of relaxation of the system dynamics into a form that is affine in the controls, and a regularization term in the performance index to ensure rigorously that the relaxed problem has the same solution as the original problem. With the appropriate choice of the independent variable, the common path constraints on heating rate, load factor and dynamic pressure all become linear inequality constraints on the altitude. Other concave inequality constraints such as those on no-fly zones are treated by successive linearization, which has been established to guarantee convergence and optimality in an SOCP setting [7]. The SOCP-based method developed in this paper proves to be a very robust and rapid tool for entry and hypersonic gliding trajectory optimization. Numerical results are provided to demonstrate the effectiveness and some of the noteworthy aspects of the method.

## II. Problem Formulation

In order for the entry trajectory optimization to be solvable by SOCP, it is crucial to formulate the optimal control problem in certain way conducive to the SOCP approach. This section presents the details of one such formulation of the problem.

### A. Trajectory Dynamics and Constraints

The non-dimensional three-degree-of-freedom (3DOF) equations of motion of an entry vehicle over a spherical rotating Earth with respect to energy are [32]

$$\begin{cases} r' = \sin \gamma / D \\ \theta' = \cos \gamma \sin \psi / r D \cos \phi \\ \phi' = \cos \gamma \cos \psi / r D \\ \gamma' = \left[ L \cos \sigma + (V^2 - 1/r) \cos \gamma / r + 2\Omega V \cos \phi \sin \psi \right. \\ \quad \left. + \Omega^2 r \cos \phi (\cos \gamma \cos \phi + \sin \gamma \cos \psi \sin \phi) \right] / V^2 D \\ \psi' = \left[ L \sin \sigma / \cos \gamma + V^2 \cos \gamma \sin \psi \tan \phi / r \right. \\ \quad \left. - 2\Omega V (\tan \gamma \cos \psi \cos \phi - \sin \phi) + \Omega^2 r \sin \psi \sin \phi \cos \phi / \cos \gamma \right] / V^2 D \end{cases} \quad (1)$$

where  $r$  is the radial distance from the center of the Earth to the vehicle,  $\theta$  and  $\phi$  are the longitude and latitude respectively,  $V$  is the Earth-relative velocity,  $\gamma$  is the relative flight-path angle, and  $\psi$  is the heading angle of the relative velocity vector, measured clockwise from the north. In these equations lengths are scaled by the radius of the Earth  $R_0 = 6378.137$  km, and time scaled by  $\sqrt{R_0/g_0}$  where  $g_0$  is the Earth gravitational acceleration at  $R_0$ . Consequently linear velocity is scaled by  $\sqrt{g_0 R_0}$ . The constant  $\Omega$  is the Earth self-rotation rate scaled by  $\sqrt{g_0/R_0}$ . The terms  $L$  and  $D$  are aerodynamic lift and drag acceleration in  $g_0$

$$L = 0.5 R_0 \rho V^2 S_{\text{ref}} C_L / m \quad (2)$$

$$D = 0.5 R_0 \rho V^2 S_{\text{ref}} C_D / m \quad (3)$$

where  $V$  is the non-dimensional velocity. But  $\rho$  is the dimensional atmospheric density which is a function of  $r$ ,  $S_{\text{ref}}$  is the dimensional reference area of the vehicle, and  $m$  is the dimensional mass of the vehicle. The lift and drag coefficients  $C_L$  and  $C_D$  are functions of the angle of attack and

Mach number. The bank angle  $\sigma$  is the rotation angle of the vehicle about the relative velocity vector.

The differentiations in Eq. (1) are with respect to the non-dimensional energy

$$e = 1/r - V^2/2 \quad (4)$$

It can be readily shown that  $e$  is monotonically increasing when the effect of Earth rotation is ignored.

$$\frac{de}{d\tau} = DV > 0 \quad (5)$$

where  $\tau$  is the non-dimensional time. The differential equation for  $V$  is not included in Eq. (1), because  $V$  can be computed at any given  $e$  and  $r$  by

$$V = \sqrt{2(1/r - e)} \quad (6)$$

During entry flight,  $r$  is very close to unity. Approximating  $r \approx 1$  in the above equation proves to be sufficiently accurate in most cases. Therefore a simpler equation for  $V$  is

$$V = \sqrt{2(1 - e)} \quad (7)$$

In this paper, a velocity-dependent angle-of-attack profile is assumed to be specified. In most entry applications the angle-of-attack is pre-determined on the basis of considerations in trim flight, thermal protection system, and downrange/crossrange requirements. Hence the physical trajectory control variable that defines the entry trajectory is the bank angle  $\sigma$ .

Let the trajectory state in Eq. (1) be  $\mathbf{x} = [r \theta \phi \gamma \psi]^T$ . The initial condition of  $\mathbf{x}$  is assumed to be given at a given initial energy  $e_0$ , i.e.,  $\mathbf{x}(e_0) = \mathbf{x}_0$ . The final energy  $e_f$  is also specified. The terminal constraints at  $e_f$  are usually the altitude (with specified final altitude and energy, the final velocity is also prescribed), and the location coordinates in terms of longitude and latitude. In addition, the final flight-path angle may be specified or desired to be with a range. For an entry vehicle that will have another phase of flight after the entry phase ends (such as the Terminal Area Energy Management phase for the Space Shuttle [28] or a terminal guidance phase), the heading angle  $\psi(e_f)$  may also be prescribed or limited within a range. Without loss of generality, we assume the following terminal constraints

$$\begin{aligned} r(e_f) &= r_f^*, \quad \theta(e_f) = \theta_f^*, \quad \phi(e_f) = \phi_f^* \\ \gamma(e_f) &= \gamma_f^*, \quad \psi(e_f) = \psi_f^* \end{aligned} \quad (8)$$

The understanding is that the last two equality constraints may be replaced by inequality constraints with given lower and upper bounds on  $\gamma(e_f)$  and/or  $\psi(e_f)$ .

Common inequality trajectory constraints include those on heating rate  $\dot{Q}$ , dynamic pressure  $\bar{q}$ , and normal load  $n$  as follows

$$\dot{Q} = k_Q \sqrt{g_0 R_0}^{3.15} \sqrt{\rho} V^{3.15} \leq \dot{Q}_{\max} \quad (9)$$

$$\bar{q} = 0.5 g_0 R_0 \rho V^2 \leq q_{\max} \quad (10)$$

$$n = \sqrt{L^2 + D^2} \leq n_{\max} \quad (11)$$

The heating rate  $\dot{Q}$ , in unit of  $\text{W/m}^2$ , is defined at a stagnation point on the surface of the vehicle with curvature radius of 0.3048 m (1 ft) and  $k_Q = 9.4369 \times 10^{-5}$ , the dynamic pressure  $\bar{q}$  is in unit of  $\text{N/m}^2$ , and the normal load  $n$  is in unit of  $g_0$ . Note that the atmospheric density  $\rho$  is a function of  $r$ , which may be reasonably approximated by an exponential function within a limited range. Since  $V$  is regarded as a function of  $e$  (cf. Eq. (7)), the constraints in Eqs. (9)–(11) can be re-expressed as

$$r(e) \geq l_Q(e), \quad r(e) \geq l_q(e), \quad r(e) \geq l_n(e) \quad (12)$$

where the limits  $l_Q$ ,  $l_q$  and  $l_n$  at a certain  $e$  can be obtained by numerically solving Eqs. (9)–(11) with “ $\leq$ ” replaced by “ $\geq$ ”. Define

$$\bar{l}(e) = \max\{l_Q(e), l_q(e), l_n(e)\} \quad (13)$$

Then, Eq. (12) is equivalent to

$$r(e) \geq \bar{l}(e) \quad (14)$$

## B. Choice of Controls

If we denote  $u = \sigma$  as the control, the state equations (1) are nonlinear in both  $\mathbf{x}$  and  $u$

$$\mathbf{x}' = \mathbf{f}(\mathbf{x}, u, e) \quad (15)$$

To apply SOCP, successive linearization will be used in Sec. III to convert the nonlinear equations into linear ones. However, it is discovered during the course of this work that linearization with respect to  $\sigma$  introduces significant high-frequency chatters in the solution profile to  $\sigma$ , and generally detrimental to the convergence of the successive solution process. To gain a quick look into the possible reason, let  $\{\mathbf{x}^k(e); u^k(e)\}$  represent the  $k$ th solution pair in the successive solution process. At the  $(k + 1)$ th iteration, the linearization of Eq. (15) yields

$$\mathbf{x}' = F_x(\mathbf{x}^k, u^k, e)\mathbf{x} + F_u(\mathbf{x}^k, u^k, e)u + \mathbf{b}(\mathbf{x}^k, u^k, e) \quad (16)$$

where  $\mathbf{b}(\mathbf{x}^k, u^k, e) = \mathbf{f}(\mathbf{x}^k, u^k, e) - F_x(\mathbf{x}^k, u^k, e)\mathbf{x}^k - F_u(\mathbf{x}^k, u^k, e)u^k$ ,  $F_x = \partial \mathbf{f} / \partial \mathbf{x}$  and  $F_u = \partial \mathbf{f} / \partial u$  are the Jacobians of  $\mathbf{f}$  with respect to  $\mathbf{x}$  and  $u$ , respectively. The coefficient matrices  $F_x$  and  $F_u$ , as well as  $\mathbf{b}$ , are not only dependent on  $\mathbf{x}^k$ , but also on  $u^k$ . In the iterative process, the control obtained in the  $k$ th iteration will affect the dynamics in Eq. (16) used to find the solution in the next iteration. Small oscillations in  $u^k$  will cause similar oscillations in the elements of the linearized dynamics. Consequently the control  $u^{k+1}$  obtained in the  $(k + 1)$ th iteration will likely exhibit and amplify the chattering effects. These high-frequency oscillations are not inherent to the problem solution, but a manifestation of numerical instability. Similar phenomena have been observed in entry trajectory optimization problems before [24, 33], as linearization will also be employed when the problem is solved as an NLP problem by a sequential quadratic programming method. The usual remedies are to add a low-pass filter to the control command or use a magnitude-limited rate command as the control. These techniques are not suitable in our problem, because the optimal bank angle in the problem will have fast switchings, as will be seen in Sec. V. The existence of such jumps in the control can be analytically proved in certain class of optimal atmospheric flight problems [34].

On the other hand, if we choose

$$u_1 = \cos \sigma, \quad u_2 = \sin \sigma \quad (17)$$

and let  $\mathbf{u} = [u_1 \ u_2]^T$  to be the control vector, the system dynamics in Eq. (1) now take the form

$$\mathbf{x}' = \mathbf{f}(\mathbf{x}, \mathbf{u}, e) = \mathbf{f}_1(\mathbf{x}, e) + B(\mathbf{x}, e)\mathbf{u} \quad (18)$$

where

$$B = \begin{bmatrix} \mathbf{0}_{3 \times 1} & \mathbf{0}_{3 \times 1} \\ (L/D)/V^2 & 0 \\ 0 & (L/D)/(V^2 \cos \gamma) \end{bmatrix} \quad (19)$$

Clearly,  $u_1$  and  $u_2$  are not independent – they must satisfy the constraint

$$u_1^2 + u_2^2 = 1 \quad (20)$$

This constraint is a quadratic equality equation and thus nonconvex. However, this difficulty can be tactically overcome by relaxing the above constraint. Details will be given in Sec. III on the relaxation technique. Linearization of Eq. (18) will result in

$$\mathbf{x}' = F_x(\mathbf{x}^k, \mathbf{u}^k, e)\mathbf{x} + B(\mathbf{x}^k, e)\mathbf{u} + \mathbf{b}(\mathbf{x}^k, \mathbf{u}^k, e) \quad (21)$$

where in this case  $\mathbf{b}(\mathbf{x}^k, \mathbf{u}^k, e) = \mathbf{f}_1(\mathbf{x}^k, e) - F_x(\mathbf{x}^k, \mathbf{u}^k, e)\mathbf{x}^k$ , and

$$F_x(\mathbf{x}, \mathbf{u}, e) = \partial \mathbf{f}(\mathbf{x}, \mathbf{u}, e) / \partial \mathbf{x} = \partial \mathbf{f}_1(\mathbf{x}, e) / \partial \mathbf{x} + \partial [B(\mathbf{x}, e)\mathbf{u}] / \partial \mathbf{x}$$

Note that the only state-dependent element in the  $B$ -matrix in Eq. (19) is through  $\cos \gamma$ , as  $L/D = C_L/C_D$  is only a function of  $V$  (thus a function of  $e$  by Eq. (7)) for a specified velocity-dependent angle of attack profile, if the weak dependence of Mach number on  $r$  is ignored. And this element will lead to the only nonzero element in  $\partial [B(\mathbf{x}, e)\mathbf{u}] / \partial \mathbf{x}$  which is proportional to  $\sin \gamma$ . In lifting entry flight  $|\gamma|$  is rather small (a fractional of one degree to a few degrees). Therefore this nonzero term is small, and may be ignored. In other words, the Jacobian  $F_x$  is nearly independent of  $\mathbf{u}$  and  $F_x \approx \partial \mathbf{f}_1(\mathbf{x}, e) / \partial \mathbf{x}$ . Thus the linearized system in Eq. (21) may be simplified to be

$$\mathbf{x}' = F_x(\mathbf{x}^k, e)\mathbf{x} + B(\mathbf{x}^k, e)\mathbf{u} + \mathbf{b}(\mathbf{x}^k, e) \quad (22)$$

Now the linearized system Eq. (22) is independent of  $\mathbf{u}^k$ . This difference between Eqs. (16) and (22) is found to be the key to suppress the undesirable high-frequency jitters in the control profile in the entry trajectory optimization problem.

It is worth noting that another benefit with the choice of controls in Eq. (17) is the convenience of imposing upper and lower bounds on the magnitude of  $\sigma$

$$\sigma_{\min} \leq |\sigma| \leq \sigma_{\max} \quad (23)$$

It is obvious that the above constraints are nonconvex. When the problem is to be eventually solved by SOCP, nonconvex constraints pose difficulty. However, if the bounds are such that  $0 \leq \sigma_{\min} < \sigma_{\max} \leq 180$  deg, the nonconvex constraints in Eq. (23) can be represented by convex (linear) constraints

$$\omega_l \leq u_1 \leq \omega_h \quad (24)$$



where  $\omega_l = \cos \sigma_{\max}$  and  $\omega_h = \cos \sigma_{\min}$ .

With  $\mathbf{u}$  defined in Eq. (17) and the Earth-rotation dependent terms separated out (which have small magnitudes), the original equations of motion (1) can be rewritten in the following concise form

$$\mathbf{x}' = \mathbf{f}_0(\mathbf{x}, e) + B(\mathbf{x}, e)\mathbf{u} + \mathbf{f}_\Omega(\mathbf{x}, e) \quad (25)$$

where

$$\mathbf{f}_0 = \begin{bmatrix} (1/D) \sin \gamma \\ \cos \gamma \sin \psi / (r D \cos \phi) \\ \cos \gamma \cos \psi / (r D) \\ (1/D - 1/r V^2 D)(\cos \gamma / r) \\ \cos \gamma \sin \psi \tan \phi / (r D) \end{bmatrix} \quad (26)$$

and  $\mathbf{f}_\Omega \in \mathbb{R}^5$  is a column vector including the terms associated with the rotation rate of the Earth. The expression of  $\mathbf{f}_\Omega$  is straightforward from Eq. (1) and is omitted here.

### C. Performance Index

In this paper, we will consider the following performance index

$$J = \int_{e_0}^{e_f} \Gamma(r, V, e) de \quad (27)$$

where  $\Gamma(r, V, e)$  is at least  $C^1$  with respect to  $r$ . A number of the commonly used performance indices in entry trajectory optimization can be cast in this form. Several examples will be given later. Other cases when the performance index involves the final coordinates  $\theta_f$ ,  $\phi_f$  and  $\psi_f$  such as in a maximum crossrange or landing footprint problem, are the subject of another forthcoming paper. In SOCP, the cost function must be linear in the optimization variables. Since  $V$  is not a state variable, this linearity condition can be met by

$$\Gamma(r, V, e) = c_1(V, e)r + c_0(V, e) \quad (28)$$

where  $c_1(V, e)$  and  $c_0(V, e)$  are functions of  $V$  and possibly  $e$ . Note that any nonlinear  $C^1$  function of  $r$  can be approximated by a first-order Taylor series expansion about a given reference profile  $r^{(k)}(e)$ . Hence a nonlinear  $\Gamma(r, V, e)$  can be approximated by the right-hand side of Eq. (28). But this is not the only possibility. For instance, when

$$\Gamma(r, V, e) = c_2(V, e)r^2 + c_1(V, e)r + c_0(V, e) \quad (29)$$

where  $c_2(V, e) > 0$  for all  $e \in [e_0, e_f]$ , it can be easily shown that the following

$$\min \int_{e_0}^{e_f} [c_2(V, e)r^2 + c_1(V, e)r + c_0(V, e)] de \quad (30)$$

is equivalent to

$$\min \int_{e_0}^{e_f} \eta de \quad (31)$$



$$\text{s.t.} \quad \left( r + \frac{c_1}{2c_2} \right)^2 \leq \frac{\eta}{c_2} + \frac{c_1^2}{4c_2^2} - \frac{c_0}{c_2} \quad (32)$$

where  $\eta$  is an auxiliary optimization variable. The constraint in Eq. (32) is a second-order cone. Once discretized, the performance index based on Eq. (31) will be linear in  $\eta$ , the inequality constraints based on Eq. (32) are second-order cones in the optimization variables, which conform with the SOCP formulation.

In the following, three commonly used performance indices in entry trajectory optimization are briefly discussed. Note that in all cases  $V$  is regarded as a function  $e$ , not a state.

1. Minimum time: The performance index with time as the independent variable is  $J = \int_{\tau_0}^{\tau_f} 1 \, d\tau$ . With  $e$  as the independent variable, the performance index becomes (cf. Eq. (5))

$$J = \int_{e_0}^{e_f} \Gamma(r, V, e) \, de = \int_{e_0}^{e_f} (1/DV) \, de \quad (33)$$

The drag acceleration  $D$  is replaced by  $D = 0.5R_0\rho V^2 S_{\text{ref}} C_D/m$ , and  $C_D$  is considered to be a function of  $V$ . The only  $r$ -dependent parameter is the atmospheric density  $\rho$ . For a given profile  $r^{(k)}(e)$ , linearizing  $1/DV$  about  $r^{(k)}(e)$  gives

$$\Gamma(r, V, e) \approx -a_0 \frac{\rho_r^{(k)}}{(\rho^{(k)})^2} r + a_0 \left( \frac{1}{\rho^{(k)}} + \frac{\rho_r^{(k)}}{(\rho^{(k)})^2} r^{(k)} \right) := c_1(V, e)r + c_0(V, e) \quad (34)$$

where  $a_0 = 2m/(R_0 S_{\text{ref}} C_D V^3)$ ,  $\rho_r$  is the derivative of atmospheric density  $\rho$  with respect to  $r$ , and the superscript  $(k)$  indicates that the corresponding parameter is evaluated along  $r^{(k)}(e)$ . Furthermore, if  $\rho$  is represented by an exponential function of  $r$  (which is a convex function of  $r$ ),  $\Gamma(r, V, e)$  is a convex function of  $r$ . Expanding  $1/DV$  in a *second-order* Taylor series about  $r^{(k)}(e)$  will lead to the form in Eq. (29)

$$\Gamma(r, V, e) \approx c_2(V, e)r^2 + c_1(V, e)r + c_0(V, e) \quad (35)$$

The convexity of  $\Gamma$  with respect to  $r$  ensures that  $c_2(V, e) > 0$  for all  $e \in [e_0, e_f]$ .

2. Minimum heat load: The performance index is  $J = \int_{\tau_0}^{\tau_f} k_0 \sqrt{\rho} V^{3.15} d\tau$  where  $k_0 = k_Q \sqrt{g_0 R_0}^{3.15} > 0$  is a constant. In terms of integration with respect to  $e$ ,

$$J = \int_{e_0}^{e_f} \Gamma(r, V, e) \, de = \int_{e_0}^{e_f} (k_0 \sqrt{\rho} V^{3.15} / DV) \, de \quad (36)$$

By following the same process as before, the integrand can be approximated by a linear form of Eq. (28) or a quadratic form of Eq. (29) with a coefficient  $c_2 > 0$  for all  $e \in [e_0, e_f]$ .

3. Maximum range: The arc length  $s$  of the trajectory on the surface of a spherical Earth is governed by  $ds/de = (V \cos \gamma / r) / DV$ . In most cases  $s$  is a reasonable approximation to the downrange traveled by an entry vehicle [28]. With  $\cos \gamma \approx 1$  and  $r \approx 1$ , the performance index for maximum range will be

$$J = \int_{e_0}^{e_f} \Gamma(r, V, e) \, de = - \int_{e_0}^{e_f} (1/D) \, de \quad (37)$$

It should be noted that if this performance index is taken, the constraints on the final longitude and latitude in Eq. (8) need to be removed to make the problem well posed. The integrand can be approximated by a linear form of Eq. (28). Note that the integrand can not be approximated as a convex quadratic form of Eq. (29), because  $-1/D$  is not convex.

The nonlinear equality constraint in Eq. (20) will be relaxed into a quadratic cone constraint in Sec. III for an SOCP formulation. To ensure that the optimal control of the relaxed problem happens on the boundary of the cone constraint so that it is equivalent to the original equality constraint in Eq. (20), modifying the performance index turns out to be an effective way. We choose to use a modified performance index

$$J = \int_{e_0}^{e_f} \Gamma(r, V, e) de + \varepsilon_\psi \int_{e_0}^{e_f} \psi de \quad (38)$$

where  $\varepsilon_\psi \neq 0$  is a constant. The magnitude of  $\varepsilon_\psi$  is set to be sufficiently small so that the solution is still very close to that of the original problem. It will be shown in Sec. III-C that under mild conditions, the presence of the second term in Eq. (38) guarantees the equivalence of the solution between the relaxed and original problems (see Remark 4 in Sec. III-C). In a sense, this small term provides *regularization* to the problem. Regularization is a commonly used mathematic technique to render a problem to possess desired properties without fundamentally changing the solution [35]. It should be pointed out that the choice of a regularization term is not unique. The presented choice is a simple one. Furthermore, it is found that if the sign of  $\varepsilon_\psi$  is selected according to the following criterion, this term helps considerably the successive solution process converge:  $\varepsilon_\psi < 0$  if the initial crossrange is positive (the target is on the right side); otherwise  $\varepsilon_\psi > 0$ .

#### D. Optimal Control Problem

Thus far with the nonlinear dynamics in Eq. (18) and constraints in Eqs. (8), (14), (20), and (24), we have a highly constrained nonlinear optimal control problem. The constraints on the final position coordinates  $\theta(e_f)$  and  $\phi(e_f)$  in Eq. (8) define the range-to-go. These hard constraints may be difficult to satisfy (e.g., the problem is infeasible) in the early iterations in the successive linearization approach within the SOCP framework to be taken in this paper. To circumvent this difficulty, these two terminal constraints in Eq. (8) on  $\theta(e_f)$  and  $\phi(e_f)$  are replaced by adding a penalty term in the performance index

$$d(\theta(e_f), \phi(e_f)) = c_\theta |\theta(e_f) - \theta_f^*| + c_\phi |\phi(e_f) - \phi_f^*| \quad (39)$$

with constants  $c_\theta > 0$  and  $c_\phi > 0$ . With this change, the infeasibility problem is avoided. Even when the target location is truly unreachable, a trajectory that ends as closely as possible to the target can still be found. The penalty term in Eq. (39) is nonlinear, but can be easily transformed into a linear function form by introducing two slack variables  $\vartheta$  and  $\varphi$ :

$$\min \bar{d}(\vartheta, \varphi) = c_\theta \vartheta + c_\phi \varphi \quad (40)$$

subject to linear inequality constraints

$$|\theta(e_f) - \theta_f^*| \leq \vartheta, \quad |\phi(e_f) - \phi_f^*| \leq \varphi \quad (41)$$

After the penalty term in Eq. (40) is incorporated into the performance index in Eq. (38), we have the following optimal control problem P0

$$\mathbf{P0}: \min \quad c_\theta \vartheta + c_\phi \phi + \int_{e_0}^{e_f} \Gamma(r, V, e) de + \varepsilon_\psi \int_{e_0}^{e_f} \psi de \quad (42)$$

$$\text{s.t.} \quad \text{Eqs. (25), (8), (14), (20), (24), (41)} \quad (43)$$

### III. Solution by Second-Order Cone Programming

In this section a solution process to Problem P0 using SOCP is presented.

#### A. Linearized Dynamics

With the choice of controls in Eq. (17), let the system dynamics be represented by Eq. (25) where for simplicity of notation we will drop the dependence on  $e$  in the symbols

$$\mathbf{x}' = \mathbf{f}_0(\mathbf{x}) + B(\mathbf{x})\mathbf{u} + \mathbf{f}_\Omega(\mathbf{x}) \quad (44)$$

The nonlinear dynamics in Eq. (44) will be approximated by linearization in the SOCP-based solution approach. Suppose that in the  $k$ th iteration the solution pair is  $\{\mathbf{x}^k(e); \mathbf{u}^k(e)\}$ , where  $\mathbf{x}^k = [r^{(k)} \ \theta^{(k)} \ \phi^{(k)} \ \gamma^{(k)} \ \psi^{(k)}]^T$  and  $\mathbf{u}^k = [u_1^{(k)} \ u_2^{(k)}]^T$ . Because the term  $\mathbf{f}_\Omega$  has a much smaller magnitude (of 2-norm), in the  $k + 1$  iteration we will approximate  $\mathbf{f}_\Omega(\mathbf{x}) \approx \mathbf{f}_\Omega(\mathbf{x}^k)$ :

$$\mathbf{x}' = \mathbf{f}_0(\mathbf{x}) + B(\mathbf{x})\mathbf{u} + \mathbf{f}_\Omega(\mathbf{x}^k) \quad (45)$$

Making use of the condition  $\partial[B(\mathbf{x})\mathbf{u}]\partial\mathbf{x} \approx 0$  as revealed in Sec. II-B, the linearization of the system in Eq. (45) about  $\{\mathbf{x}^k; \mathbf{u}^k\}$  gives

$$\mathbf{x}' = A(\mathbf{x}^k)\mathbf{x} + B(\mathbf{x}^k)\mathbf{u} + \mathbf{b}(\mathbf{x}^k) \quad (46)$$

where

$$A(\mathbf{x}^k) = \frac{\partial \mathbf{f}_0}{\partial \mathbf{x}}(\mathbf{x}^k) = \begin{bmatrix} -\frac{D_r^{(k)} \sin \gamma^{(k)}}{(D^{(k)})^2} & 0 & 0 & \frac{\cos \gamma^{(k)}}{D^{(k)}} & 0 \\ a_{21} & 0 & \frac{\cos \gamma^{(k)} \sin \psi^{(k)} \sin \phi^{(k)}}{r^{(k)} D^{(k)} \cos^2 \phi^{(k)}} & -\frac{\sin \gamma^{(k)} \sin \psi^{(k)}}{r^{(k)} D^{(k)} \cos \phi^{(k)}} & \frac{\cos \gamma^{(k)} \cos \psi^{(k)}}{r^{(k)} D^{(k)} \cos \phi^{(k)}} \\ a_{31} & 0 & 0 & -\frac{\sin \gamma^{(k)} \cos \psi^{(k)}}{r^{(k)} D^{(k)}} & -\frac{\cos \gamma^{(k)} \sin \psi^{(k)}}{r^{(k)} D^{(k)}} \\ a_{41} & 0 & 0 & \frac{\sin \gamma^{(k)}}{D^{(k)} r^{(k)}} \left( \frac{1}{r^{(k)} (V^{(k)})^2} - 1 \right) & 0 \\ a_{51} & 0 & \frac{\cos \gamma^{(k)} \sin \psi^{(k)}}{r^{(k)} D^{(k)} \cos^2 \phi^{(k)}} & -\frac{\sin \gamma^{(k)} \sin \psi^{(k)} \tan \phi^{(k)}}{r^{(k)} D^{(k)}} & \frac{\cos \gamma^{(k)} \cos \psi^{(k)} \tan \phi^{(k)}}{r^{(k)} D^{(k)}} \end{bmatrix}$$

and

$$\mathbf{b}(\mathbf{x}^k) = \mathbf{f}_0(\mathbf{x}^k) - A(\mathbf{x}^k)\mathbf{x}^k + \mathbf{f}_\Omega(\mathbf{x}^k) \quad (47)$$

In  $A(\mathbf{x}^k)$ ,  $D^{(k)} = D(\mathbf{x}^k)$ ,  $D_r^{(k)} = \partial D(\mathbf{x}^k)/\partial r$ , and

$$a_{21} = -\left( \frac{D_r^{(k)}}{r^{(k)} (D^{(k)})^2} + \frac{1}{(r^{(k)})^2 D^{(k)}} \right) \frac{\cos \gamma^{(k)} \sin \psi^{(k)}}{\cos \phi^{(k)}}$$

$$\begin{aligned}
 a_{31} &= -\left(\frac{D_r^{(k)}}{r^{(k)}(D^{(k)})^2} + \frac{1}{(r^{(k)})^2 D^{(k)}}\right) \cos \gamma^{(k)} \cos \psi^{(k)} \\
 a_{41} &= \frac{D_r^{(k)} \cos \gamma^{(k)}}{(D^{(k)})^2 r^{(k)}} \left(\frac{1}{r^{(k)}(V^{(k)})^2} - 1\right) + \frac{\cos \gamma^{(k)}}{D^{(k)}(r^{(k)})^2} \left(\frac{2}{r^{(k)}(V^{(k)})^2} - 1\right) \\
 a_{51} &= -\cos \gamma^{(k)} \sin \psi^{(k)} \tan \phi^{(k)} \left(\frac{D_r^{(k)}}{r^{(k)}(D^{(k)})^2} + \frac{1}{(r^{(k)})^2 D^{(k)}}\right)
 \end{aligned}$$

To ensure the validity of linearization, a trust-region constraint is imposed as follows

$$|\mathbf{x} - \mathbf{x}^k| \leq \delta \quad (48)$$

where  $\delta \in \mathbb{R}^5$  is a constant vector and the inequality “ $\leq$ ” in the above equation applies component-wise, that is,  $|x_i - x_i^{(k)}| \leq \delta_i$  for  $i = 1, \dots, 5$ .

## B. Relaxation of Control Constraints

The original control set determined by the control constraints in Eqs. (20) and (24) is shown in the first plot of Fig. 1, which is two circular arcs on the unit circle between  $u_1 = \omega_l$  and  $u_1 = \omega_h$ . This set is obviously nonconvex, unsuitable for application of any convex optimization technique. Linearizing Eq. (20) would give the control set a convex approximation, but the result will depend on  $\mathbf{u}^k$ , and the high-frequency chattering phenomenon observed in Sec. II-B will appear again. Another common convexification scheme is to relax a nonconvex constraint to expand its feasible set, so that the relaxed constraint becomes convex. In this paper, we relax the equality constraint in Eq. (20) into the inequality constraint

$$u_1^2 + u_2^2 \leq 1 \quad (49)$$

Now the relaxed control set determined by the control constraints in Eqs. (24) and (49) is convex, as shown by the shaded area in the second plot of Fig. 1. However, if the optimal control of the relaxed problem with the constraint in Eq. (49) lies in the interior of the constraint set, it is not the solution of the original problem, and the solution would be useless. Therefore, the major challenge associated with the relaxation technique is to make sure that the optimal control of the relaxed problem is on the boundary of the constraint in Eq. (49), namely, the constraint in Eq. (49) is required to be active at the solution point. Such an assurance will be provided in the following subsection.

## C. Assurance of Active Control Constraint

With the nonlinear dynamics in Eq. (44) replaced by Eqs. (46)–(48) after linearization and relaxation of the constraint in Eq. (20) by Eq. (49), we attempt to find the solution to Problem P0 defined in Eqs. (42) and (43) by solving the following sequence of convex optimal control problems for  $k = 0, 1, 2, \dots$

$$\mathbf{P1:} \min \quad c_\theta \vartheta + c_\phi \varphi + \int_{e_0}^{e_f} \Gamma(r, V, e) de + \varepsilon_\psi \int_{e_0}^{e_f} \psi de \quad (50)$$

$$\text{s.t.} \quad \mathbf{x}' = A(\mathbf{x}^k) \mathbf{x} + B(\mathbf{x}^k) \mathbf{u} + \mathbf{b}(\mathbf{x}^k), \quad \mathbf{x}(e_0) = \mathbf{x}_0 \quad (51)$$

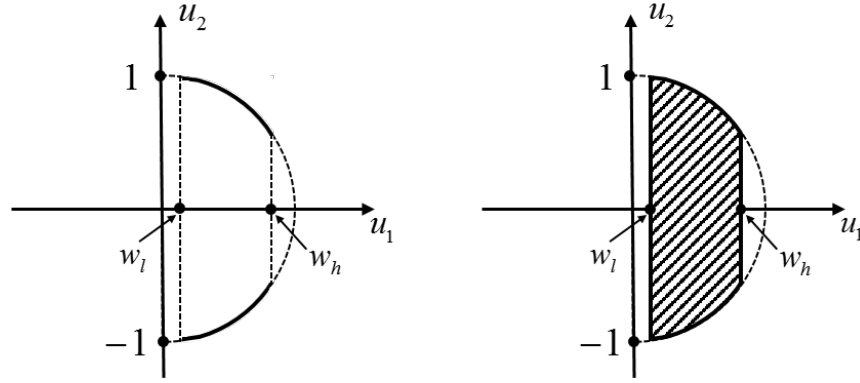


**Figure 1** Relaxation of control set: (Left) original nonconvex set: two solid arc segments on the semicircle; (Right) relaxed convex set: shaded area plus its boundaries.

$$|\mathbf{x}(e) - \mathbf{x}^k(e)| \leq \delta \quad (52)$$

$$u_1^2(e) + u_2^2(e) \leq 1 \quad (53)$$

$$\omega_l \leq u_1(e) \leq \omega_h \quad (54)$$

$$r(e) \geq \bar{l}(e) \quad (55)$$

$$|\theta(e_f) - \theta_f^*| \leq \vartheta, \quad |\phi(e_f) - \phi_f^*| \leq \varphi \quad (56)$$

$$r(e_f) = r_f^*, \quad \gamma(e_f) = \gamma_f^*, \quad \psi(e_f) = \psi_f^* \quad (57)$$

Let the solution to the above problem be  $\mathbf{x}^{k+1}$ . This successive solution process is considered to have converged if

$$|\mathbf{x}^{k+1}(e) - \mathbf{x}^k(e)| \leq \epsilon, \quad \forall e \in [e_0, e_f] \quad (58)$$

where  $\epsilon \in \mathbb{R}^5$  is a constant tolerance vector and the inequality is applied component-wise.

The objective of this section is to establish rigorously that the constraint of Eq. (53) in Problem P1 is always active, i.e.,

$$u_1^2(e) + u_2^2(e) = 1, \quad \forall e \in [e_0, e_f] \quad (59)$$

With the condition in Eq. (59), the converged solution of Problem P1 is also the solution of Problem P0.

We first introduce two mild assumptions:

#### Assumption 1

The trust region constraint in Eq. (52) is always inactive, i.e.,  $|\mathbf{x}(e) - \mathbf{x}^k(e)| < \delta$ ,  $\forall e \in [e_0, e_f]$ .

#### Assumption 2

If the constraint in Eq. (54) is active over a finite interval  $[e_1, e_2] \subset [e_0, e_f]$ , i.e., either  $u_1(e) = \omega_l$  or  $u_1(e) = \omega_h$ ,  $\forall e \in [e_1, e_2]$ , the constraint in Eq. (55) is inactive in  $[e_1, e_2]$ .

#### Remark 1:

Assumption 1 is almost always satisfied as long as the process of solving Problem P1 does not diverge and a sufficiently large constant vector  $\delta$  is chosen.

*Remark 2:*

Note that the constraint in Eq. (55) is equivalent to the constraints on heating rate, dynamic pressure, and normal load in Eqs. (9)–(11). When the constraint in Eq. (55) is active in a finite interval, the controls required to maintain the trajectory on the boundary of the constraint is generally not constant, therefore cannot be equal to  $\omega_l$  or  $\omega_h$ . Hence Assumption 2 is more a statement of fact than an imposing assumption.

Throughout this paper when a property is said to hold “almost everywhere (a.e.)”, it means that this condition may be violated only at a finite number of points (a set of measure zero). The central result of this section is stated below:

*Proposition 1*

Let  $\{\mathbf{x}^*(e); \mathbf{u}^*(e); \vartheta^*; \varphi^*\}$  be the solution of Problem P1 over a fixed interval  $[e_0, e_f]$ . Then, under Assumptions 1 and 2,  $[u_1^*(e)]^2 + [u_2^*(e)]^2 = 1$  is satisfied a.e. on  $[e_0, e_f]$ .

*Proof:* See the Appendix.

*Remark 3:*

Proposition 1 establishes that the solution to Problem P1 is a valid approximate solution to Problem P0. The only approximation is in the linearization of the dynamic equations. Note that Proposition 1 is valid for any  $\Gamma(r, V, e)$  that is  $C^1$  with respect to  $r$ . In addition, it is found through numerical examples that  $[u_1^*(e)]^2 + [u_2^*(e)]^2 = 1$  is satisfied at all discretized points on  $[e_0, e_f]$  except that it may not be satisfied at points where the bank reversals occur. But the possibility that the condition  $[u_1^*(e)]^2 + [u_2^*(e)]^2 = 1$  does not hold at isolated points does not affect the validity of Proposition 1.

*Remark 4:*

From the proof in the Appendix, it can be seen that the regularization term  $\varepsilon_\psi \int_{e_0}^{e_f} \psi de$  in the performance index in Eq. (50) (which comes from Eq. (38)) plays an instrumental role. Without this term (e.g.,  $\varepsilon_\psi = 0$ ), a critical result in the proof will not hold. Indeed, numerical experiments also verify that in the absence of this term, the solution to Problem P1 will in many cases result in  $[u_1^*(e)]^2 + [u_2^*(e)]^2 < 1$ .

*Remark 5:*

Proposition 1 also remains valid if an additional constraint of the following form is imposed to Problem P1 (and P0)

$$r \leq r_{\max}(e) \quad (60)$$

where  $r_{\max}$  is an upper bound (possibly dependent on  $e$ ) on  $r$ . Such a constraint can arise from the desire to limit the altitude along the trajectory below a certain level. The equilibrium-glide constraint in the Shuttle entry guidance design [28] imposes a lower bound on the drag acceleration, which can be translated into an altitude ceiling at each velocity. This constraint will be in the form of Eq. (60).

In Ref. [36] a similar lossless convexification result on non-convex inequality constraint on the control vector is proved for linear systems subject to state inequality constraints. The difference is that the integral term in the performance index in Ref. [36] is a function of only the control vector

whereas the performance in Problem P1 here is a nonlinear function of longitudinal state variables and  $\psi$  as defined in Eq. (50). This is an important consequential difference that necessitates different proof of the equivalence of the solutions to Problems P0 and P1.

#### D. Discretization and the Solution Procedure

In this section, the state equations in Eq. (51) in Problem P1 will be discretized at  $N + 1$  uniformly distributed discretized points in  $[e_0, e_f]$  and all other constraints are enforced at these points. When the independent variable  $e$  is divided into a uniform grid of  $N$  points, the step size is  $\Delta e = (e_f - e_0)/N$ , and the discretized points can be denoted as  $\{e_0, e_1, e_2, \dots, e_N\}$  with  $e_i = e_0 + i\Delta e$ ,  $i = 0, 1, \dots, N$ . Then, the state  $\mathbf{x}$  and control  $\mathbf{u}$  in Problem P1 are discretized by  $\mathbf{x}_i = \mathbf{x}(e_i)$  and  $\mathbf{u}_i = \mathbf{u}(e_i)$ . The state equations in Eq. (51) can be numerically integrated by the trapezoidal rule as follows:

$$\mathbf{x}_i = \mathbf{x}_{i-1} + \frac{\Delta e}{2} \left[ (A_{i-1}^k \mathbf{x}_{i-1} + B_{i-1}^k \mathbf{u}_{i-1} + \mathbf{b}_{i-1}^k) + (A_i^k \mathbf{x}_i + B_i^k \mathbf{u}_i + \mathbf{b}_i^k) \right], \quad i = 1, 2, \dots, N \quad (61)$$

where  $A_i^k = A(\mathbf{x}^k(e_i))$ ,  $B_i^k = B(\mathbf{x}^k(e_i))$ , and  $\mathbf{b}_i^k = \mathbf{b}(\mathbf{x}^k(e_i))$ . After rearrangement, Eq. (61) is further rewritten as

$$H_{i-1} \mathbf{x}_{i-1} - H_i \mathbf{x}_i + G_{i-1} \mathbf{u}_{i-1} + G_i \mathbf{u}_i = -\frac{\Delta e}{2} (\mathbf{b}_{i-1}^k + \mathbf{b}_i^k) \quad (62)$$

where  $H_{i-1} = I + \frac{\Delta e}{2} A_{i-1}^k$ ,  $H_i = I - \frac{\Delta e}{2} A_i^k$ ,  $G_{i-1} = \frac{\Delta e}{2} B_{i-1}^k$ ,  $G_i = \frac{\Delta e}{2} B_i^k$ , and  $I$  is a unit matrix with the same dimension as that of  $A$ . The variables  $\{\mathbf{x}_0, \dots, \mathbf{x}_N\}$  and  $\{\mathbf{u}_0, \dots, \mathbf{u}_N\}$ , along with the slack variables  $\vartheta$  and  $\varphi$  in the cost function, are considered to be optimization variables, which can be linked together as an optimization variable vector  $\mathbf{z} = [\mathbf{x}_0^T \dots \mathbf{x}_N^T \mathbf{u}_0^T \dots \mathbf{u}_N^T \vartheta \varphi]^T$ . The collection of the discretized state equations at all  $e_i$  forms a linear algebraic system in  $\mathbf{z}$

$$M\mathbf{z} = F \quad (63)$$

where

$$M = \begin{bmatrix} I & 0 & 0 & 0 & 0 & 0 & 0 & 0 & 0 & 0 & 0 & 0 & 0_{1 \times 2} \\ H_0 & H_1 & 0 & \dots & 0 & 0 & G_0 & G_1 & 0 & \dots & 0 & 0 & 0_{1 \times 2} \\ \vdots & \vdots & \vdots & \ddots & \vdots & \vdots & \vdots & \vdots & \vdots & \ddots & \vdots & \vdots & \vdots \\ 0 & 0 & 0 & \dots & H_{N-1} & H_N & 0 & 0 & 0 & \dots & G_{N-1} & G_N & 0_{1 \times 2} \end{bmatrix}$$

$$F = -\frac{\Delta e}{2} \begin{bmatrix} -\frac{2}{\Delta e} \mathbf{x}_0 \\ \mathbf{b}_0^k + \mathbf{b}_1^k \\ \vdots \\ \mathbf{b}_{N-1}^k + \mathbf{b}_N^k \end{bmatrix}$$

where the first block row of Eq. (63) actually represents the specified initial condition  $\mathbf{x}(e_0) = \mathbf{x}_0$ . The integrand  $\Gamma(r, V, e)$  in Eq. (50) is also linearized about  $\mathbf{x}^k$ , and the performance index in Eq. (50) is also discretized into a linear function of  $\mathbf{z}$ , denoted by  $\mathbf{c}^T \mathbf{z}$  with  $\mathbf{c}$  being a constant vector for



each fixed  $k$ . Thus a discretized version of Problem P1 is given as Problem P2 in the following

$$\begin{aligned} \mathbf{P2:} \quad & \min \quad \mathbf{c}^T \mathbf{z} \\ & \text{s.t.} \quad \mathbf{Mz} = \mathbf{F} \end{aligned} \quad (64)$$

$$|\mathbf{x}_i - \mathbf{x}_i^k| \leq \delta \quad (65)$$

$$\|\mathbf{u}_i\| \leq 1, \omega_l \leq (u_1)_i \leq \omega_h \quad (66)$$

$$r_i \geq \bar{l}_i \quad (67)$$

$$|\theta_N - \theta_f^*| \leq \vartheta, |\phi_N - \phi_f^*| \leq \varphi \quad (68)$$

$$r_N = r_f^*, \gamma_N = \gamma_f^*, \psi_N = \psi_f^* \quad (69)$$

where  $\mathbf{x}_i = [r_i \ \theta_i \ \phi_i \ \gamma_i \ \psi_i]^T$ ,  $\mathbf{u}_i = [(u_1)_i \ (u_2)_i]^T$ ,  $\|\cdot\|$  is the 2-norm, and  $i = 0, 1, \dots, N$ .

Problem P2 is an SOCP problem, as it has a linear cost function, and all constraints are either second-order constraints (Eq. (66)), or linear constraints. Assuming that the discretization is sufficiently accurate so that the solution of the SOCP problem P2 is a close approximation of the solution to Problem P1, Proposition 1 assures that the condition  $[(u_1)_j]^2 + [(u_2)_j]^2 = 1$  (or  $\|\mathbf{u}_j\| = 1$ ) will hold in the solution of Problem P2.

When the integrand  $\Gamma(r, V, e)$  is approximated by a second-order approximation in Eq. (29), the vector  $\mathbf{z}$  will include the discretized values of an additional variable  $\eta$  as in Eq. (31) and additional second-order cone constraints at  $e_i$  from Eq. (32) will be in Problem P2. But P2 will remain an SOCP problem.

The dimension of Problem P2 will be large when hundreds of nodes are used in the discretization process. But the coefficient matrix  $\mathbf{M}$  in Eq. (64) is a sparse matrix. This is a feature which the state-of-the-art primal-dual interior-point method [18] will take full advantage of to efficiently solve the problem.

The algorithm to find the solution to Problem P0 is summarized as follows:

1. Set  $k = 0$ , and choose an initial state profile  $\mathbf{x}^0$ .
2. At the  $(k + 1)$ th iteration ( $k \geq 0$ ), use  $\mathbf{x}^k$  to set up Problem P2 by defining  $\mathbf{M}$  and  $\mathbf{F}$  in Eq. (64),  $\mathbf{x}_i^k$  in the trust region constraint, and  $\bar{l}_i$  in the path constraint. Then, solve Problem P2 to get its solution. Denote the solution as  $\mathbf{z}^{k+1} = \{\mathbf{x}^{k+1}; \mathbf{u}^{k+1}; \vartheta^{k+1}; \varphi^{k+1}\}$ .
3. Check whether the following convergence condition is satisfied

$$\max_i |\mathbf{x}_i^{k+1} - \mathbf{x}_i^k| \leq \epsilon \quad (70)$$

where the “ $\leq$ ” is a component-wise inequality and  $\epsilon \in \mathbb{R}^5$  is a user-defined sufficiently small constant vector. If the above condition is met, go to Step 4; otherwise, replace  $\mathbf{z}^k$  with  $\mathbf{z}^{k+1}$ , set  $k = k + 1$ , and go back to Step 2.

4. The solution for P0 is found to be  $\mathbf{z}^{k+1}$ . Stop.

*Remark 6:*

In Step 1, we only need to provide an initial state profile  $\mathbf{x}^0$ , but not  $\mathbf{u}^0$ ,  $\vartheta^0$ , and  $\varphi^0$  in the optimization vector  $\mathbf{z}$ . The solution process is not sensitive to the choice of  $\mathbf{x}^0$ . For example,

we can choose the flight-path angle profile to be a small constant value such as  $-0.1$  deg, the longitude/latitude profile be a straight line from the initial location to the target location, and the heading angle profile be also a straight line connecting its initial value and the required terminal value. To determine the initial altitude profile, we integrate the equations of motion from the initial conditions with zero bank angle until the flight-path angle changes from negative to positive for the first time, and denote the altitude at this moment by  $r_1$ . Then a complete initial  $r$ -profile is the altitude profile from the integration plus a straight line from  $r_1$  to  $r_f^*$ .

On the other hand, no user-supplied initial guess to the optimization vector  $\mathbf{z}$  is required.

*Remark 7:*

A rigorous proof of the convergence of the sequence of problems P2 is not yet available, although each Problem P2 is guaranteed to have an optimal solution if there is an interior point that satisfies all the inequality constraints – this is the so-called *Slater's condition* [12]. The proof of convergence of the sequence of the problems P2 is likely to remain an open challenge, given the nonlinear, nonconvex, and highly constrained nature of Problem P0. However, with the formulation in this paper, extensive numerical tests have been performed successfully that instill confidence in the convergence. The solution process is typically rapid and robust.

#### IV. No-Fly Zones

An no-fly zone (NFZ) may be modeled as a cylinder with its center at the specified longitude and latitude and a given radius. An NFZ constraint then limits the longitude and latitude of the trajectory by

$$(\theta - \theta_c)^2 + (\phi - \phi_c)^2 \geq d^2 \quad (71)$$

where  $\theta_c$  and  $\phi_c$  are the longitude and latitude of the center of the NFZ, and  $d$  is the radius of the NFZ in radian. When necessary, the NFZ constraint is added to Problem P0. The constraint (71) is a concave constraint and thus nonconvex. In Ref. [7], it is shown that in an optimization problem which is otherwise convex if the concave constraints are discounted, the concave constraints can be approximated successively by its linearized form. This successive linearization process is guaranteed to converge under mild conditions, and the converged solution is at least a local minimum of the problem. The reader is referred to Refs. [7] and [9] for more detail. In this paper, the same approach is used to add the linearized NFZ constraint to Problem P1

$$2(\theta^{(k)} - \theta_c)\theta + 2(\phi^{(k)} - \phi_c)\phi \geq d^2 + \bar{d} \quad (72)$$

where  $\theta^{(k)}$  and  $\phi^{(k)}$  are from the solution in the  $k$ th iteration, and

$$\bar{d} = -(\theta^{(k)} - \theta_c)^2 - (\phi^{(k)} - \phi_c)^2 + 2(\theta^{(k)} - \theta_c)\theta^{(k)} + 2(\phi^{(k)} - \phi_c)\phi^{(k)}$$

Then, the linear constraint in Eq. (72) is discretized and added to Problem P2. Problem P2 is still an SOCP, and the solution process proceeds as before. The technical question is whether this addition of the constraint in Eq. (72) will change the conclusion in Proposition 1. To answer this question, the following assumption is needed.

*Assumption 3*

Along the optimal trajectory, if the NFZ constraint in Eq. (72) becomes active, it is active only at isolated points in  $[e_0, e_f]$ .

We are now ready to state the following conclusion:

*Proposition 2*

For the problem P1 with the constraint (72) included, let  $\{\mathbf{x}^*(e); \mathbf{u}^*(e); \vartheta^*; \varphi^*\}$  be an optimal solution over a fixed interval  $[e_0, e_f]$ . Then, under Assumption 1, Assumption 2, and Assumption 3,  $[u_1^*(e)]^2 + [u_2^*(e)]^2 = 1$  is satisfied a.e. on  $[e_0, e_f]$ .

*Proof:* When the constraint in Eq. (72) is added to Problem P1, there will be an additional term in the construction of the Lagrangian  $L$  in Eq. (A10). Nevertheless, under Assumption 3, the costate equations are still the same as those for Problem P1, because this additional term is zero almost everywhere. There will be no jump conditions in the costates  $p_\theta$  and  $p_\phi$  which remain continuous in  $[e_0, e_f]$ . Therefore, the same proof for Proposition 1 in the Appendix still applies.

*Remark 8:*

Unlike low-speed vehicles such as unmanned aerial vehicles (UAVs), at hypersonic speeds it is very difficult for an entry vehicle to maintain a constant-radius turn as required to fly along the boundary of the NFZ constraint. This is because an entry vehicle has a much smaller aerodynamic lift coefficient than a UAV and the lateral force required to make a tight turn at hypersonic speeds is very large. The entry trajectory usually at most touches the boundary of an NFZ constraint at a point. Hence Assumption 3 is not nearly as restrictive as it may seem.

*Remark 9:*

The conclusions in this section and the same solution procedure readily apply when there are multiple NFZ constraints.

## V. Numerical Demonstrations

In this section, the models of a reusable launch vehicle X-33 [37] and a hypersonic gliding vehicle dubbed common aero vehicle (CAV-H) [38] will be used to demonstrate the algorithm proposed in Sec. III. The X-33 has a medium  $L/D$  ratio of about 0.8, while the CAV-H has a hypersonic  $L/D$  ratio of about 3.5. A nominal angle of attack profile for the X-33, shown in the first plot of Fig. 2, is used [37], and a nominal angle of attack profile corresponding to the maximum lift-to-drag ratio of CAV [32] is shown in the second plot of Fig. 2.

For both X-33 and CAV-H, the trust region constraint in Eq. (65) is selected as

$$|\mathbf{x} - \mathbf{x}^k| \leq \boldsymbol{\delta} = \left[ \frac{20000}{R_0} \quad \frac{20\pi}{180} \quad \frac{20\pi}{180} \quad \frac{20\pi}{180} \quad \frac{70\pi}{180} \right]^T$$

where  $\mathbf{x} = [r \ \theta \ \phi \ \gamma \ \psi]^T$  as defined before. This bound of the trust region is sufficiently large to satisfy Assumption 1. In the stopping criteria in Eq. (70), we select

$$\boldsymbol{\epsilon} = \left[ \frac{200}{R_0} \quad \frac{0.05\pi}{180} \quad \frac{0.05\pi}{180} \quad \frac{0.05\pi}{180} \quad \frac{0.05\pi}{180} \right]^T$$

In all applications in this section, a value of  $N = 200$  is used in the discretization as described in Sec. III-D. The MATLAB modeling environment YALMIP [39] is used to call a state-of-the-art primal-dual interior-point method in the software MOSEK [18] to solve the SOCP problems P2. All the results are obtained by running the algorithm on a desktop with Intel Core i7-3370 3.40 GHz.

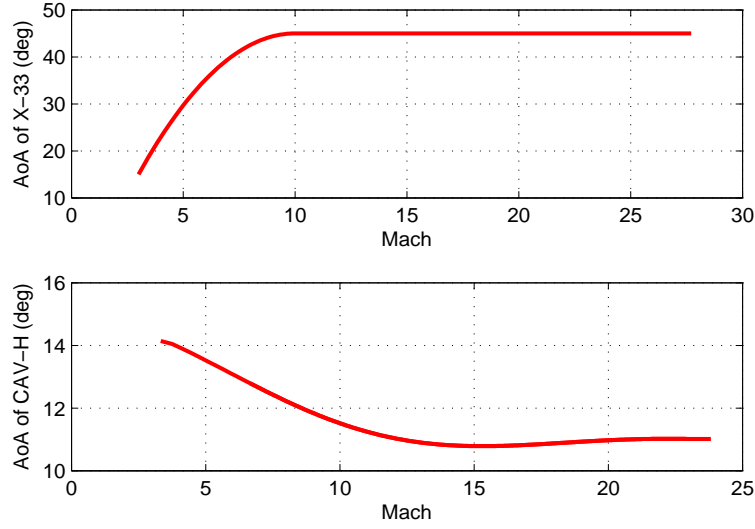


**Figure 2** Nominal angle of attack profiles for X-33 and CAV-H.

### A. Minimum-Time Entry Trajectory of X-33

For this mission the initial condition at the entry interface and the terminal condition are given in Table 1. Based on the data, this mission has an initial downrange of 7454 km and left crossrange of 701 km. The terminal flight-path angle can be any value in the range  $[-6, 0]$  deg and the terminal heading angle must be 90 deg, pointing to the due east. The values of the limits in the path constraints in Eqs. (9)–(11) are as follows:  $\dot{Q}_{\max} = 800 \text{ kW/m}^2$ ,  $\bar{q}_{\max} = 14,364 \text{ N/m}^2$ , and  $n_{\max} = 2.5(g_0)$ . In addition, the lower and upper bounds on the magnitude of the bank angle in Eq. (23) are set at  $\sigma_{\min} = 15 \text{ deg}$  and  $\sigma_{\max} = 165 \text{ deg}$ .

**Table 1** The initial and terminal conditions for X-33

States	$r(\text{km})$	$V(\text{m/s})$	$\gamma(^{\circ})$	$\theta(^{\circ})$	$\phi(^{\circ})$	$\psi(^{\circ})$
$\mathbf{x}_0$	121.9	7626	-1.2493	237	-25	45
$\mathbf{x}_f$	30.48	908.15	$[-6, 0]$	279	28.61	90

The performance index is the time of flight, with  $\Gamma(r, V)$  in the form of Eq. (34). Upon discretization, the total number of optimization variables is 1409. The total number of constraints is 3826, including, among others, 1005 equality constraints from the system dynamics in Eq. (64), 2010 inequality constraints from the trust-region constraint in Eq. (65), 603 inequality constraints from the control constraints in Eq. (66), and 201 inequality constraints from the path constraints in Eq. (67).

The converged complete solution takes 6 successive iterations (Step 2 in the algorithm outlined in Sec. III-D) to obtain. In each successive iteration, it takes IPMs an average of 0.14 second to solve the Problem P2 in Sec. III-D. The altitude profiles in the first 4 iterations are plotted in Fig. 3 and it can be seen that the altitude profile in the 4th iteration is already almost indiscernible from that in the 3rd iteration to the scale of the plot.

To verify the SOCP-based method developed in this work, numerical results are compared with those obtained by an open-source optimal control software written in C++ called PSOPT [40]. PSOPT uses direct collocation methods. The default NLP solver employed by PSOPT is another interior-point algorithm called IPOPT [41]. In addition to the minimum-time problem, the maximum-time problem is also solved under identical conditions and constraints. The PSOPT solutions use the Legendre pseudospectral discretization, with the ODE-error tolerance set to  $10^{-3}$  in the mesh refinement procedure. The trajectory profiles by the SOCP-based method and PSOPT are shown in Figs. 4–6, and the times of flight and the CPU times required are given in Table 2. The SOCP and PSOPT solutions match quite well, based on the figures. The trajectory controls (bank angle) and other profiles in Figs. 4–6 are very similar both qualitatively and quantitatively. The relatively small differences in flight times could be attributable to the different discretization schemes used in the two solution approaches. Good initial guesses are required for PSOPT to converge, though. The impressive solution speed of the SOCP-based approach may still be further improved by a customized IPM [42].

One can see in Fig. 4 the typical high-frequency jitters in the bank angle history for the minimum-time trajectory obtained by PSOPT, a phenomenon often observed in entry optimization problems [24, 33]. But with the formulation in this paper, the SOCP-based solution no longer suffers from the same problem. It is also rather interesting to note that the bank angle profiles of the minimum-time trajectory (both SOCP and PSOPT solutions) exhibit an instantaneous change of the sign around 1020 seconds. In entry guidance terminology, this is called “bank reversal” which is commanded by a separate lateral logic [28]. Here the optimal solution automatically converges on such a profile without a separate logic to command such a sign change. This is also why adding a low-pass filter or using magnitude-limited rate command as the control in this class of problems is not suitable (cf. the discussion in Sec. II-B). In certain cases with appropriate simplifications, it can actually be proved that discontinuity in the optimal bank angle profile is an inherent part of the optimal solution [34].

Figure 5 shows the trajectories in altitude-velocity space. The minimum-time trajectory is generally lower, much of it is along the boundaries of the heating rate and normal load constraints. Figure 6 confirms that the heating rate constraint in Eq. (9) is active along both minimum- and maximum-time trajectories which have total heat load of  $149.4 \text{ KWh/m}^2$  ( $537.9 \text{ MWs/m}^2$ ) and  $150.0 \text{ KWh/m}^2$  ( $540.1 \text{ MWs/m}^2$ ) respectively, and the normal load constraint in Eq. (11) is active along the minimum-time trajectory. Such characteristics are dictated by the performance index of minimum time: the trajectory seeks to dissipate the energy at the fastest pace allowed by the down-range requirement and path constraints. The maximum-time trajectory seeks to do the opposite.

**Table 2** Comparison of the minimum- and maximum-time solutions for X33

Solution	Time of flight (sec)	CPU time (sec)
min-time solution by SOCP	1214	0.84
min-time solution by PSOPT	1225	46.26
max-time solution by SOCP	1344	1.54
max-time solution by PSOPT	1377	13.87

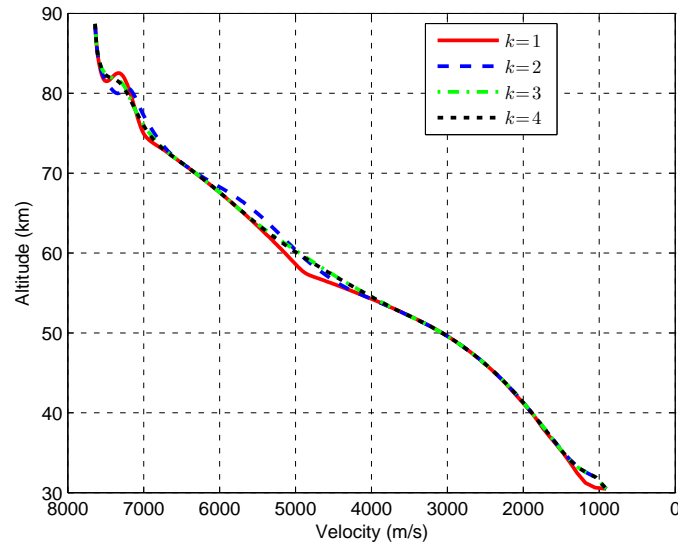


**Figure 3** Altitude profiles in the first 4 successive iterations of the algorithm for minimum-time entry of X-33.

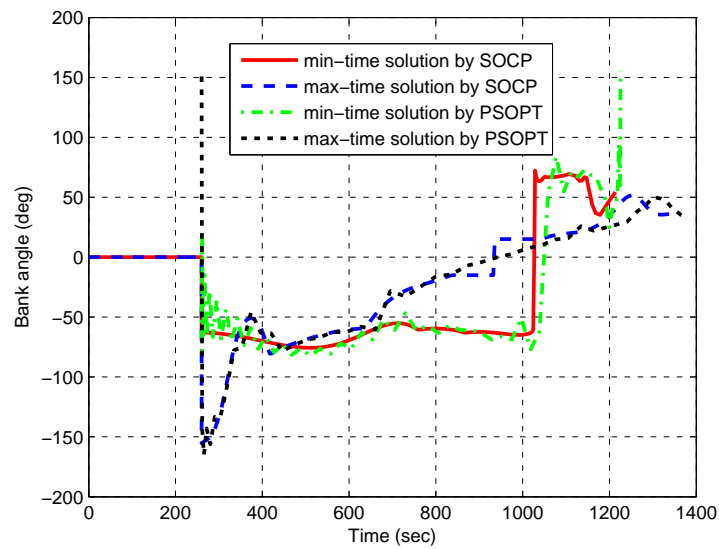


**Figure 4** Bank angle histories for minimum-time and maximum-time entry of X-33.

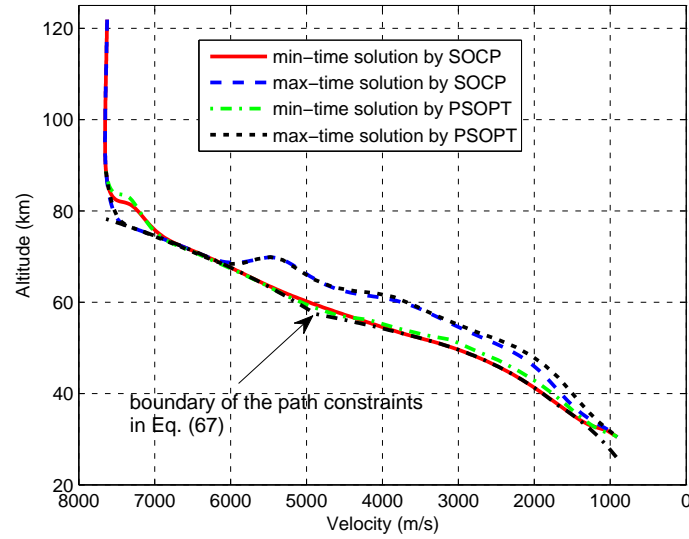


**Figure 5** Altitude histories for minimum-time and maximum-time entry of X-33.

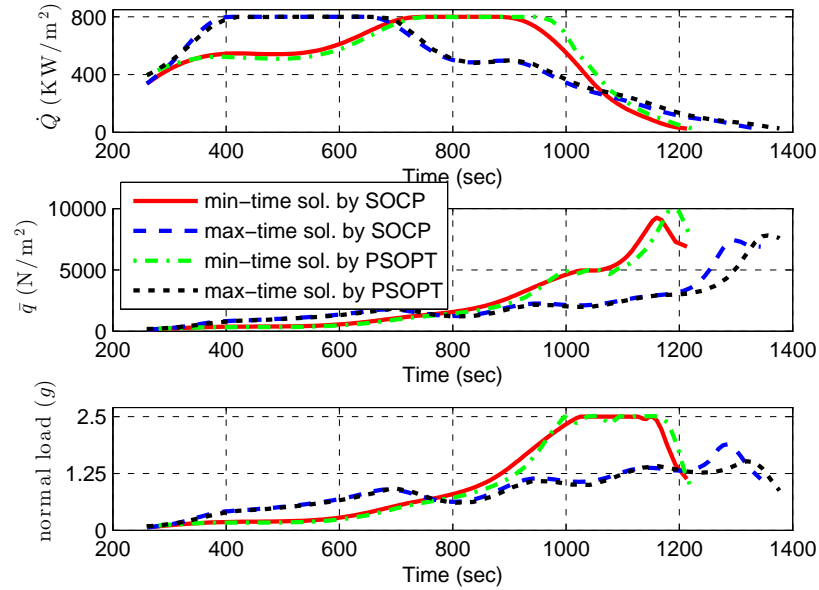


**Figure 6** Heating rate, dynamic pressure, and normal load histories for minimum-time and maximum-time entry of X-33.



## B. Minimum-Heat-Load Entry Trajectory of X-33

Depending on the type of thermal protection system, the primary thermal concern can be in total heat load or peak heating rate. Suppose that the performance index is to minimize the integrated heat load for the X-33. The initial and terminal conditions are the same as given in Table 1, and the same path constraint limits on heating rate, dynamic pressure and normal load as given in Sec. V.A are imposed.

The altitude history-vs-velocity is shown in Fig. 7, and the heating rate and normal load versus velocity are shown in Fig. 8 (the dynamic pressure is not plotted, because the constraint on it was not active.) The bank angle profile is given in Fig. 9. Compared to the minimum-time solution, it is evident that the strategy for incurring the smallest heat load is to dive deeper into the atmosphere and glide along the boundary of the path constraints, by commanding a large bank angle right after the entry interface. Such a strategy results in a loss in downrange when the vehicle is subject to increased drag. But the range loss is made up by flying at a higher altitude above the boundary of the path constraints later, as can be clearly seen in Fig. 7. The history of the heat load (at the stagnation point) along the optimal trajectory is plotted in Fig. 10. The total heat load is  $147.3 \text{ KWh/m}^2$  ( $530.1 \text{ MWs/m}^2$ ) along the minimum-heat-load trajectory. In contrast, the minimum-time solution has a heat load of  $149.4 \text{ KWh/m}^2$  ( $537.9 \text{ MWs/m}^2$ ) which is just about 1.5% higher. Figure 9 confirms that two solutions are sufficiently close to each other with similar pattern in the bank-angle profiles.

Lastly, it is worth pointing out that the normal load constraint becomes active twice along the minimum-heat-load trajectory as seen in Fig. 8. This is an advantage of direct method in that the user does not have to face the difficulty to guess the patterns of active inequality trajectory constraints in the optimal solution, and lay out the necessary conditions accordingly as is the case in applying the indirect approach, which can be a rather tedious and trial-and-error process [25,26].

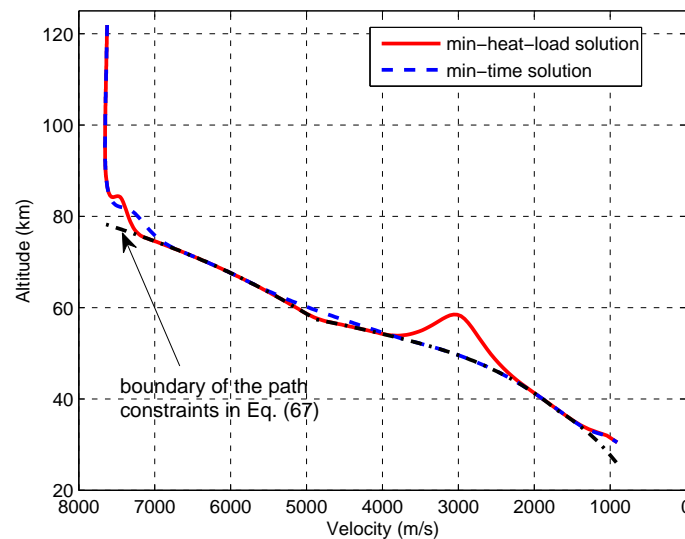


**Figure 7** Altitude histories for minimum-heat-load and minimum-time entry of X-33.

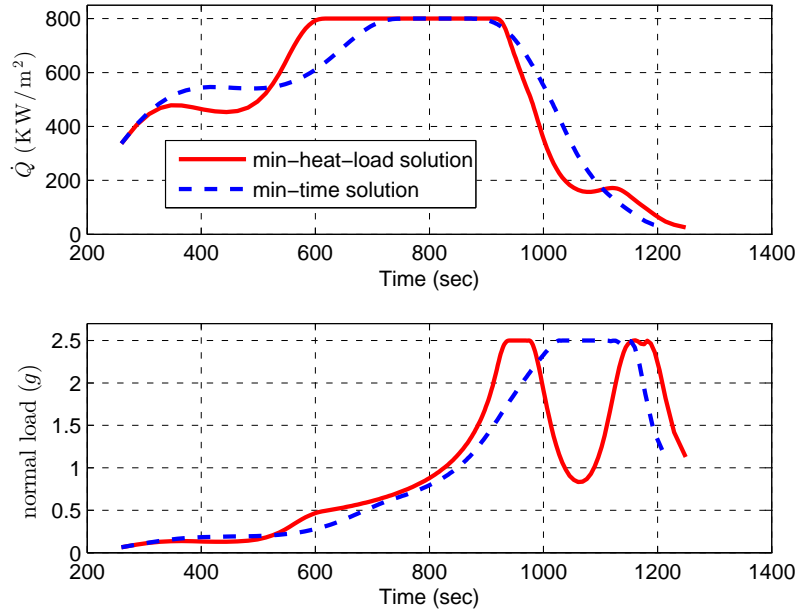


**Figure 8** Heating rate and normal load histories for minimum-heat-load and minimum-time entry of X-33.

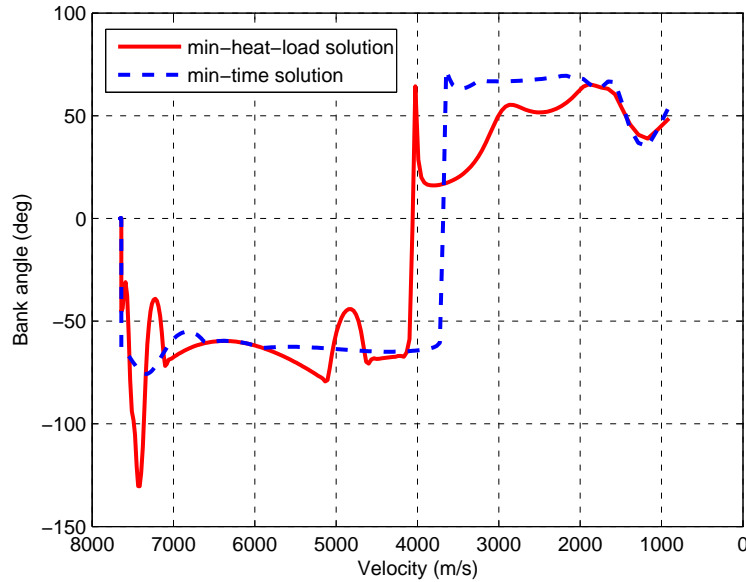


**Figure 9** Bank angle histories for minimum-heat-load and minimum-time entry of X-33.

### C. Minimum-Time Entry of CAV with No-Fly Zone Constraints

The initial and terminal conditions of the mission for a *minimum-time* mission for the CAV-H are given in Table 3. The target has an initial downrange of 14,661 km and left crossrange of 735 km. The inequality trajectory constraint limits are as follows:  $\dot{Q}_{\max} = 4,000 \text{ kW/m}^2$ ,  $\bar{q}_{\max} = 70,000 \text{ N/m}^2$ , and  $n_{\max} = 2.5(g_0)$ . In addition, two NFZ constraints are present and the parameters are given in Table 4.

Since the CAV-H has a much higher  $L/D$  ratio than the X-33, the entry trajectory will likely to

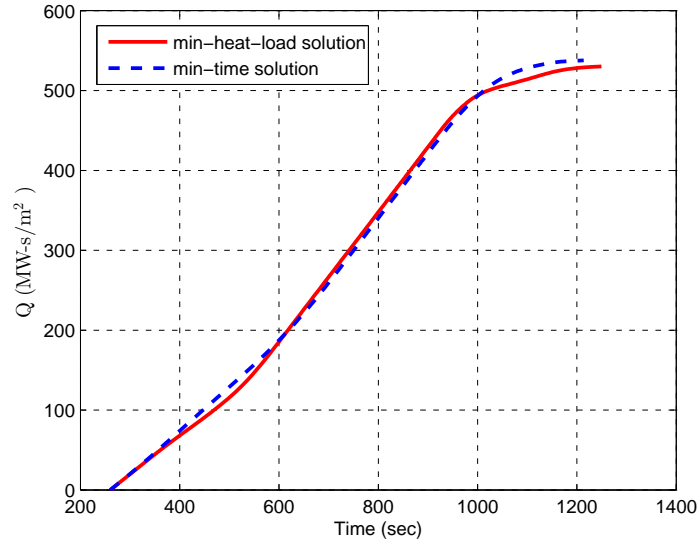


**Figure 10** Heat load histories for minimum-heat-load and minimum-time entry of X-33.

**Table 3** Initial and terminal conditions for orbital entry of CAV-H

States	$r(\text{km})$	$V(\text{m/s})$	$\gamma(^{\circ})$	$\theta(^{\circ})$	$\phi(^{\circ})$	$\psi(^{\circ})$
$x_0$	121.9	7400	-1	120	-40	61.39
$x_f$	28	2000	0	230	50	50

have large phugoid oscillations [32]. To limit the phugoid oscillations, a lower bound on the drag acceleration is imposed after the CAV-H enters the dense atmosphere

$$0.1 (g) \leq D \quad (73)$$

With the velocity regarded as a function of  $e$ , this constraint is equivalent to an  $e$ -dependent *upper* bound on  $r$  as in Eq. (60).

When the NFZ constraints are imposed, the final heading angle is not tightly constrained, but allowed to vary in a range of

$$30 \text{ deg} \leq \psi_f \leq 70 \text{ deg} \quad (74)$$

The ground track of the solution subject to the NFZ constraints is shown in Fig. 11. For comparison the minimum-time solution for the CAV-H in the same mission but without the NFZ constraints is also obtained. The trajectory without NFZ constraints flies through both NFZs,

**Table 4** Center and radius of the NFZ 1 and NFZ 2

NFZ #	Center ( $\theta, \phi$ )	Radius (km)
NFZ 1	(171°, -10°)	1,002 (540 nm)
NFZ 2	(210°, 32°)	1,446 (780 nm)

while the trajectory with the NFZ constraints grazes the two NFZs (and Assumption 3 in Sec. IV is satisfied). The corresponding bank angle profiles are given in Fig. 12. It is interesting to note that to steer away from NFZ 1, the trajectory has to fly a large negative bank angle initially, in contrast to positive initial bank angle along the trajectory without the NFZ constraints. The two NFZ constraints cause the trajectory to use 157 more seconds in flight time as compared to the trajectory without the NFZ constraints. Again, bank-reversal-like rapid changes of the sign of the bank angle are present.

The heating rate and dynamic pressure histories are plotted in Fig. 13 (the normal load constraint is not active thus not plotted). Both the heating rate and dynamic pressure constraints are active, with or without the NFZ constraints. Still, the maneuvers to satisfy the NFZ constraints have visible influence on the when and how the inequality constraints on heating rate and dynamic pressure constraints become active (the dynamic pressure constraint becomes active twice along the trajectory subject to the NFZ constraints).

Figure 14 shows the altitude-vs-range profiles. The constraint in Eq. (73) is essential in keeping the trajectories from having large phugoid oscillations. Figure 15 is even more illustrative: the lower bound in the drag acceleration in Eq. (73) is active for first 1700 seconds, especially for the trajectory without the NFZ constraints. Without this constraint, the altitude would have much higher peaks at the same velocities, hence much smaller drag acceleration.

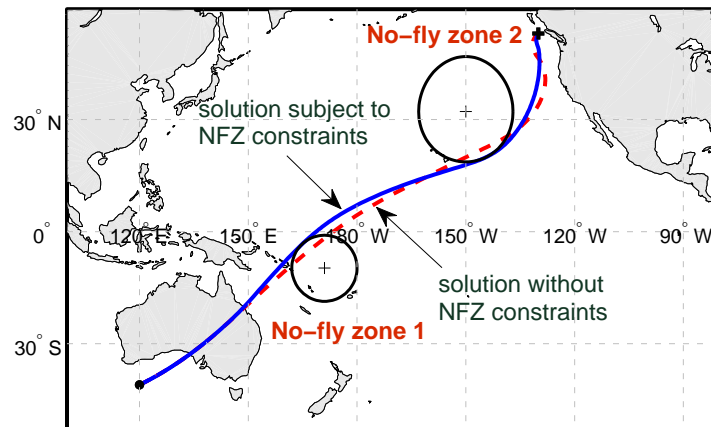


**Figure 11** Ground tracks for the orbital entry mission of CAV-H.

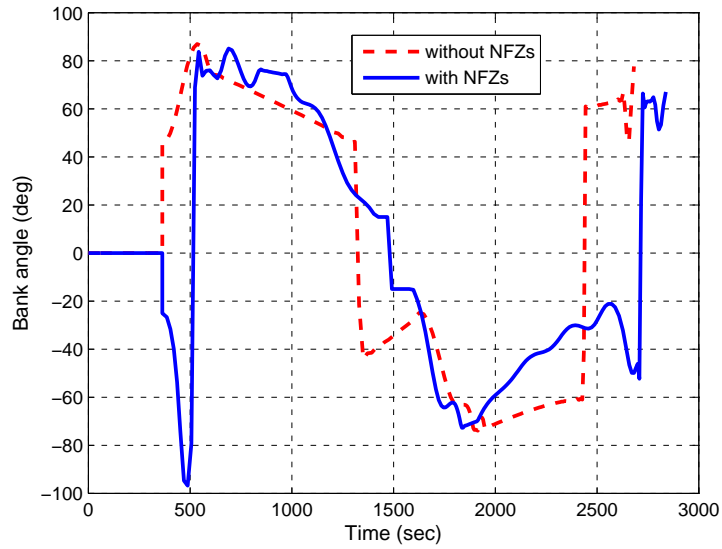


**Figure 12** Bank angle histories for the orbital entry mission of CAV-H.

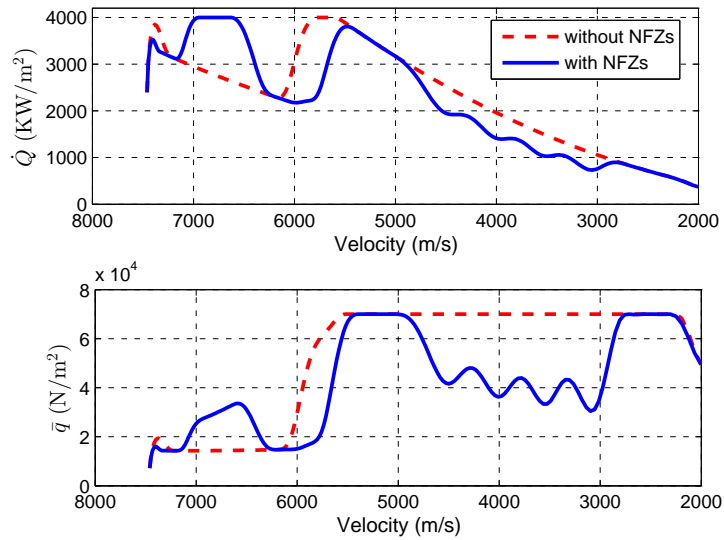


**Figure 13** Heating rate and normal load histories for the orbital entry mission of CAV-H.

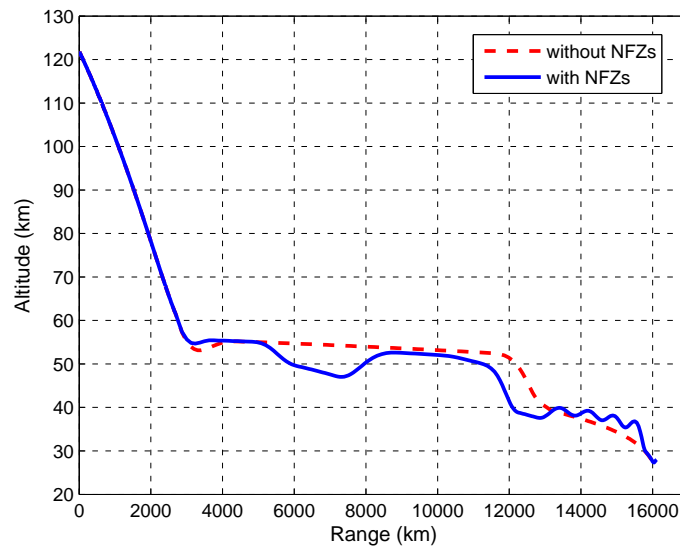


**Figure 14** Altitude-vs-range histories for the orbital entry mission of CAV-H.

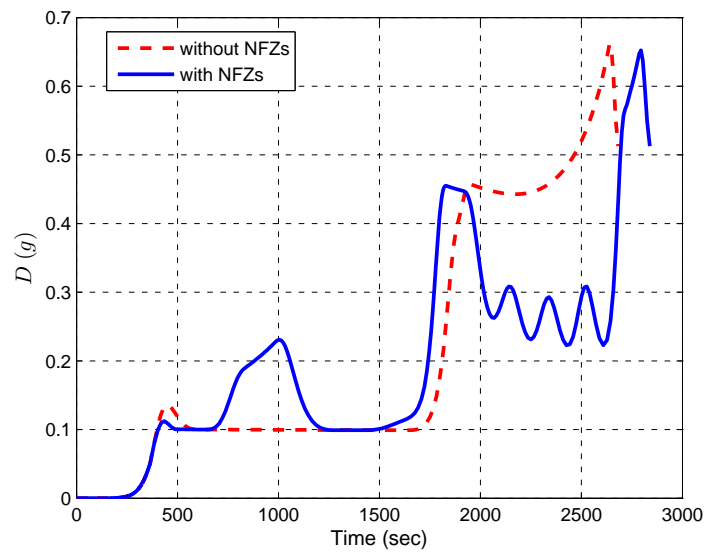


**Figure 15** Drag acceleration histories for the orbital entry mission of CAV-H.

## **VI. Conclusions**

Applications of convex optimization in aerospace trajectory planning and optimization have been limited to problems without complex nonlinear dynamics and aerodynamic forces so far. In this paper, a successive second-order cone programming (SOCP) based method is proposed to solve a class of highly constrained entry trajectory optimization problems. The standard linearization and control augmentation (by using the rate of an input as the control) techniques often employed to “convexify” nonlinear, non-convex dynamics do not work well for the entry trajectory optimization problem. The focus of this paper is on how to formulate the problem so that the SOCP based approach can be successfully applied. A systematic procedure is developed in this paper in which the solution to the entry trajectory optimization problem is found by solving a sequence of carefully cast problems. Each of these subproblems, upon discretization, is solved as an SOCP problem. Rigorous analysis is carried out to establish that each of these subproblems is a valid approximation to the original problem. The computational performance of the proposed approach proves to be very competitive.

Aside from offering an appealing addition to the existing toolbox for entry trajectory planning and optimization, this paper represents an attempt in expanding the applications of modern convex optimization to more challenging and practical aerospace engineering problems. New technical issues will arise and solutions will be required along the way, whether they are generic or specific to a class of problems. This work contributes to the continually increased understanding and knowledge in this endeavor.

## **Acknowledgment**

The first author acknowledges the support to this research by China Postdoctoral Science Foundation (Grant No.: 2014M550592).



## Appendix: Proof of Proposition 1

To apply the standard optimal control theory to Problem P1, we first introduce slack variables  $\xi_1$ ,  $\xi_2$ ,  $\eta_1$ , and  $\eta_2$ , and construct an optimal control problem equivalent to P1 as follows:

$$\begin{aligned} \bar{\mathbf{P1}} : \min \quad & c_\theta \xi_1(e_f) + c_\phi \xi_2(e_f) + \int_{e_0}^{e_f} \Gamma(r, V) de + \varepsilon_\psi \int_{e_0}^{e_f} \psi de \\ \text{s.t.} \quad & \mathbf{x}' = A(\mathbf{x}^k) \mathbf{x} + B(\mathbf{x}^k) \mathbf{u} + \mathbf{b}(\mathbf{x}^k), \mathbf{x}(e_0) = \mathbf{x}_0 \end{aligned} \quad (\text{A1})$$

$$[\xi_1(e)]' = \eta_1(e), \xi_1(e_0) = 0 \quad (\text{A2})$$

$$[\xi_2(e)]' = \eta_2(e), \xi_2(e_0) = 0 \quad (\text{A3})$$

$$u_1^2(e) + u_2^2(e) \leq 1 \quad (\text{A4})$$

$$\omega_l \leq u_1(e) \leq \omega_h \quad (\text{A5})$$

$$r(e) \geq \bar{l}(e) \quad (\text{A6})$$

$$|\theta(e_f) - \theta_f^*| \leq \xi_1(e_f), |\phi(e_f) - \phi_f^*| \leq \xi_2(e_f) \quad (\text{A7})$$

$$r(e_f) = r_f^*, \gamma(e_f) = \gamma_f^*, \psi(e_f) = \psi_f^* \quad (\text{A8})$$

Note that  $\vartheta$  and  $\varphi$  in P1 are equivalent to  $\xi_1(e_f)$  and  $\xi_2(e_f)$  in  $\bar{\mathbf{P1}}$  respectively. When Assumption 1 holds, Problems P1 and  $\bar{\mathbf{P1}}$  are mathematically equivalent. Now Problem  $\bar{\mathbf{P1}}$  is a standard optimal control problem with  $\{\mathbf{x}(e), \xi_1(e), \xi_2(e)\}$  as the state and  $\{\mathbf{u}(e), \eta_1(e), \eta_2(e)\}$  as the control.

We apply the Maximum Principle to Problem  $\bar{\mathbf{P1}}$  by using the direct adjoining approach [43]. A note of caution is that Ref. [43] states the necessary conditions for the maximization of the performance index in the optimal control problem. Define the Hamiltonian  $H$  and Lagrangian  $L$  as follows:

$$\begin{aligned} H = & p_r(a_{11}r + a_{14}\gamma + b_1) + p_\theta(a_{21}r + a_{23}\phi + a_{24}\gamma + a_{25}\psi + b_2) \\ & + p_\phi(a_{31}r + a_{34}\gamma + a_{35}\psi + b_3) + p_\gamma \left( a_{41}r + a_{44}\gamma + b_4 + \frac{(L/D)^{(k)}}{(V^{(k)})^2} u_1 \right) \\ & + p_\psi \left( a_{51}r + a_{53}\phi + a_{54}\gamma + a_{55}\psi + b_5 + \frac{(L/D)^{(k)}}{(V^{(k)})^2 \cos \gamma^{(k)}} u_2 \right) \\ & + p_{\xi_1} \eta_1 + p_{\xi_2} \eta_2 + p_0 \Gamma(r, V) + p_0 \varepsilon_\psi \psi \end{aligned} \quad (\text{A9})$$

$$L = H + \mu_u(1 - u_1^2 - u_2^2) + \mu_l(u_1 - \omega_l) + \mu_h(\omega_h - u_1) + \nu(r - \bar{l}) \quad (\text{A10})$$

where  $p_0 \leq 0$  is a constant,  $\mathbf{p}(e) = [p_r(e) \ p_\theta(e) \ p_\phi(e) \ p_\gamma(e) \ p_\psi(e) \ p_{\xi_1}(e) \ p_{\xi_2}(e)]^T \in \mathbb{R}^7$  is the costate vector, and  $\mu_u(e)$ ,  $\mu_l(e)$ ,  $\mu_h(e)$ ,  $\nu(e) \in \mathbb{R}$  are the Lagrangian multipliers. Let  $a_{ij}(e)$  and  $b_i(e)$  be the nonzero elements of  $A(\mathbf{x}^k(e))$  and  $\mathbf{b}(\mathbf{x}^k(e))$  respectively in Eq. (A1). Note that the dependence on  $e$  in all variables is dropped for simplicity. In addition, we define  $\Phi$  as

$$\begin{aligned} \Phi = & p_0[c_\theta \xi_1(e_f) + c_\phi \xi_2(e_f)] + \zeta[r(e_f) - \bar{l}(e_f)] \\ & + \lambda_\theta[\theta(e_f) - \theta_f^* + \xi_1(e_f)] + \lambda_\theta^+[-\theta(e_f) + \theta_f^* + \xi_1(e_f)] \\ & + \lambda_\phi[\phi(e_f) - \phi_f^* + \xi_2(e_f)] + \lambda_\phi^+[-\phi(e_f) + \phi_f^* + \xi_2(e_f)] \\ & + \lambda_r[r(e_f) - r_f^*] + \lambda_\gamma[\gamma(e_f) - \gamma_f^*] + \lambda_\psi[\psi(e_f) - \psi_f^*] \end{aligned} \quad (\text{A11})$$

where  $\zeta$ ,  $\lambda_\theta^-$ ,  $\lambda_\theta^+$ ,  $\lambda_\phi^-$ ,  $\lambda_\phi^+$ ,  $\lambda_r$ ,  $\lambda_\gamma$ , and  $\lambda_\psi$  are all constants.

If  $\{\mathbf{x}^*(e), \xi_1^*(e), \xi_2^*(e); \mathbf{u}^*(e), \eta_1^*(e), \eta_2^*(e)\}$  is an optimal solution for  $\overline{\text{PI}}$  over a fixed interval  $[e_0, e_f]$  and the optimal trajectory  $\{\mathbf{x}^*(e), \xi_1^*(e), \xi_2^*(e)\}$  is assumed to have only finitely many junction times, the following conditions hold almost everywhere [43]:

1) the nontriviality condition:

$$(p_0, \mathbf{p}(e), \nu(e), \lambda_\theta^-, \lambda_\theta^+, \lambda_\phi^-, \lambda_\phi^+) \neq 0, \quad \forall e \in [e_0, e_f] \quad (\text{A12})$$

2) the pointwise maximum condition: along the optimal trajectory  $\{x^*(e), \xi_1^*(e), \xi_2^*(e)\}$  and the corresponding costate  $\mathbf{p}(e)$ , the optimal control  $\{u_1^*(e), u_2^*(e), \eta_1^*(e), \eta_2^*(e)\}$  is determined by

$$\{u_1^*, u_2^*, \eta_1^*, \eta_2^*\} = \arg \max_{(u_1, u_2) \in \mathcal{U}} H(\mathbf{x}^*, \xi_1^*, \xi_2^*, u_1, u_2, \eta_1, \eta_2, \mathbf{p}) \quad (\text{A13})$$

where  $\mathcal{U} = \{(u_1, u_2) | u_1^2 + u_2^2 \leq 1, \omega_l \leq u_1 \leq \omega_h\}$ .

3) the costate differential equations ( $\mathbf{p}' := d\mathbf{p}/de = -\partial_{\mathbf{x}}L$ ):

$$p'_r = -a_{11}p_r - a_{21}p_\theta - a_{31}p_\phi - a_{41}p_\gamma - a_{51}p_\psi - p_0\partial_r\Gamma(r, V) - \nu \quad (\text{A14})$$

$$p'_\theta = 0 \quad (\text{A15})$$

$$p'_\phi = -a_{23}p_\theta - a_{53}p_\psi \quad (\text{A16})$$

$$p'_\gamma = -a_{14}p_r - a_{24}p_\theta - a_{34}p_\phi - a_{44}p_\gamma - a_{54}p_\psi \quad (\text{A17})$$

$$p'_\psi = -a_{25}p_\theta - a_{35}p_\phi - a_{55}p_\psi - p_0\varepsilon_\psi \quad (\text{A18})$$

$$p'_{\xi_1} = 0, \quad p'_{\xi_2} = 0 \quad (\text{A19})$$

4) the complementary slack conditions:

$$\mu_u \geq 0, \quad \mu_u[1 - (u_1^*)^2 - (u_2^*)^2] = 0 \quad (\text{A20})$$

$$\mu_l \geq 0, \quad \mu_l(u_1^* - \omega_l) = 0 \quad (\text{A21})$$

$$\mu_h \geq 0, \quad \mu_h(\omega_h - u_1^*) = 0 \quad (\text{A22})$$

$$\nu \geq 0, \quad \nu(r^* - \bar{l}) = 0 \quad (\text{A23})$$

$$\zeta \geq 0, \quad \zeta[r^*(e_f) - \bar{l}(e_f)] = 0 \quad (\text{A24})$$

$$\lambda_\theta^- \geq 0, \quad \lambda_\theta^-[\theta^*(e_f) - \theta_f^* + \xi_1(e_f)] = 0 \quad (\text{A25})$$

$$\lambda_\theta^+ \geq 0, \quad \lambda_\theta^+[-\theta^*(e_f) + \theta_f^* + \xi_1(e_f)] = 0 \quad (\text{A26})$$

$$\lambda_\phi^- \geq 0, \quad \lambda_\phi^-[\phi^*(e_f) - \phi_f^* + \xi_2(e_f)] = 0 \quad (\text{A27})$$

$$\lambda_\phi^+ \geq 0, \quad \lambda_\phi^+[-\phi^*(e_f) + \phi_f^* + \xi_2(e_f)] = 0 \quad (\text{A28})$$

5) the transversality conditions (only the ones that will be used in this paper are given):

$$p_{\xi_1}(e_f) = \partial_{\xi_1}\Phi = p_0c_\theta + \lambda_\theta^- + \lambda_\theta^+ \quad (\text{A29})$$

$$p_{\xi_2}(e_f) = \partial_{\xi_2}\Phi = p_0c_\phi + \lambda_\phi^- + \lambda_\phi^+ \quad (\text{A30})$$

Proof of Proposition 1:

Under Assumption 1,  $\overline{P1}$  is equivalent to P1 mathematically. Suppose the optimal solution  $\{\mathbf{x}^*(e); \mathbf{u}^*(e); \vartheta^*; \varphi^*\}$  in P1 has the corresponding optimal solution  $\{\mathbf{x}^*(e), \xi_1^*(e), \xi_2^*(e); \mathbf{u}^*(e), \eta_1^*(e), \eta_2^*(e)\}$  as in  $\overline{P1}$ . Then, all optimality conditions in Eqs. (A12)–(A30) apply.

In the following, we will first prove  $[u_1^*(e)]^2 + [u_2^*(e)]^2 = 1$  holds on intervals where none of the conditions  $u_1^*(e) = \omega_l$  and  $u_1^*(e) = \omega_h$  is satisfied, and then prove  $[u_1^*(e)]^2 + [u_2^*(e)]^2 = 1$  also holds on intervals where one of the conditions  $u_1^*(e) = \omega_l$  and  $u_1^*(e) = \omega_h$  is satisfied, all by contradiction.

*Case 1:* consider any finite interval  $[e_1, e_2] \subset [e_0, e_f]$  where none of the conditions  $u_1^*(e) = \omega_l$  and  $u_1^*(e) = \omega_h$  is satisfied.

In this case, the constraint (A5) is not active and can thus be ignored, plus any term related to it in those optimality conditions above. Assume that there exists an interval  $[e_i, e_j] \subset [e_1, e_2]$  with  $e_i < e_j$  such that  $[u_1^*(e)]^2 + [u_2^*(e)]^2 < 1$ . We will argue that this is impossible by deriving a condition violating the nontriviality condition in Eq. (A12).

With the hypothesis that  $[u_1^*(e)]^2 + [u_2^*(e)]^2 < 1$  in  $[e_i, e_j]$ , Eq. (A20) implies that  $\mu_u(e) = 0$ ,  $\forall e \in [e_i, e_j]$ . In the following discussion, the dependence of variables on  $e$  is omitted for simplicity, but the reader should keep in mind that the discussion is on the interval  $[e_i, e_j]$ , unless indicated otherwise. First, it is easy to see that the Hamiltonian  $H$  defined in Eq. (A9) is a linear function of the controls  $\eta_1$  and  $\eta_2$ . Because  $\eta_1$  and  $\eta_2$  are not constrained, maximization of  $H$  with respect to them is infinity unless their associated coefficients  $p_{\xi_1}$  and  $p_{\xi_2}$  are both zero over the whole interval  $[e_0, e_f]$ , so we have  $p_{\xi_1} = p_{\xi_2} = 0$ .

In addition, the pointwise maximum condition (A13) has its first-order necessary conditions of optimality (or KKT conditions) as  $\partial_{u_1} L = 0$  and  $\partial_{u_2} L = 0$ , i.e.,

$$\frac{(L/D)^{(k)}}{(V^{(k)})^2} p_\gamma - 2\mu_u u_1 = 0 \quad (\text{A31})$$

$$\frac{(L/D)^{(k)}}{(V^{(k)})^2 \cos \gamma^{(k)}} p_\psi - 2\mu_u u_2 = 0 \quad (\text{A32})$$

Since  $\mu_u = 0$ , the above two equations imply that  $p_\gamma = p_\psi = 0$ . Substituting  $p_\psi = 0$  into the costate differential equations for  $p_\phi$  and  $p_\psi$  in Eqs. (A16) and (A18) respectively, we have

$$p'_\phi = -a_{23} p_\theta \quad (\text{A33})$$

$$0 = -a_{25} p_\theta - a_{35} p_\phi - p_0 \varepsilon_\psi \quad (\text{A34})$$

where the value of  $a_{35}$  (see Eq. (46) for its explicit expression) is zero only when the heading  $\psi = 0$  or  $\pi$ , which implies that  $a_{35}$  is nonzero a.e. on  $[e_0, e_f]$ . When  $a_{35} \neq 0$ , solving for  $p_\phi$  from Eq. (A34) yields

$$p_\phi = -\frac{a_{25}}{a_{35}} p_\theta - \frac{p_0 \varepsilon_\psi}{a_{35}} \quad (\text{A35})$$

which is, then, substituted into Eq. (A33) to get

$$\left[ \left( -\frac{a_{25}}{a_{35}} \right)' + a_{23} \right] p_\theta - \varepsilon_\psi \left( \frac{1}{a_{35}} \right)' p_0 = 0 \quad (\text{A36})$$

where  $p'_\theta = 0$  in Eq. (A15) is used and the superscript (') means derivative with respect to  $e$ . From the above equation, we can obtain

$$p_\theta = \varepsilon_\psi \alpha p_0 \quad (\text{A37})$$

where

$$\alpha = \frac{(1/a_{35})'}{-(a_{25}/a_{35})' + a_{23}} \quad (\text{A38})$$

Since there is no jump on  $p_\theta$ , Eq. (A15) implies that  $p_\theta$  must be a constant on the whole interval  $[e_0, e_f]$ . Hence, we require  $\varepsilon_\psi \alpha p_0$  to be a constant as well based on Eq. (A37). What we already know is that  $\varepsilon_\psi$  is a nonzero constant and  $p_0$  is a non-positive constant. The variable  $\alpha$ , defined in Eq. (A38), is time-varying and not a constant. If  $p_0 < 0$ , it becomes obvious that  $\varepsilon_\psi \alpha p_0$  must not be a constant, which will contradict Eq. (A37) since  $p_\theta$  is a constant. Therefore, we must have  $p_0 = 0$ , which then gives  $p_\theta = 0$  from Eq. (A37). Substituting  $p_0 = p_\theta = 0$  into Eq. (A35), we get  $p_\phi = 0$ .

We have already proven  $p_0 = p_\theta = p_\phi = p_\gamma = p_\psi = p_{\xi_1} = p_{\xi_2} = 0$ . Next, we will prove  $p_r = \nu = 0$  and  $\lambda_\theta^- = \lambda_\theta^+ = \lambda_\phi^- = \lambda_\phi^+ = 0$ . It is easy to see that the costate differential equation for  $p_\gamma$  in Eq. (A17) directly yields  $p_r = 0$  since all other variables in the equation are zero. Consequently, we can get  $\nu = 0$  from the costate equation for  $p_r$  in Eq. (A14). Then, the transversality conditions in Eqs. (A29) and (A30), combined with  $p_0 = p_{\xi_1} = p_{\xi_2} = 0$ , imply  $\lambda_\theta^- = \lambda_\theta^+ = \lambda_\phi^- = \lambda_\phi^+ = 0$ , since  $\lambda_\theta^- \geq 0$ ,  $\lambda_\theta^+ \geq 0$ ,  $\lambda_\phi^- \geq 0$ , and  $\lambda_\phi^+ \geq 0$  are given in Eqs. (A25)–(A28).

Up to now, we have proven  $p_0 = \mathbf{p} = \nu = \lambda_\theta^- = \lambda_\theta^+ = \lambda_\phi^- = \lambda_\phi^+ = 0$ , which contradicts the nontriviality condition in Eq. (A12). Therefore, there exists no finite interval  $[e_i, e_j]$  over which  $[u_1^*(e)]^2 + [u_2^*(e)]^2 < 1$  is satisfied.

*Case 2:* consider any finite interval  $[e_1, e_2] \subset [e_0, e_f]$  where one of the conditions  $u_1^*(e) = \omega_l$  and  $u_1^*(e) = \omega_h$  is satisfied.

In this case, a similar (but identical) analysis of the necessary conditions together with  $u_1^*(e) = \omega_l$  or  $\omega_h$  (constant) rules out the possibility of  $[u_1^*(e)]^2 + [u_2^*(e)]^2 < 1$ . Details are omitted here.

In summary, it has been proved that  $[u_1^*(e)]^2 + [u_2^*(e)]^2 = 1$  a.e. on  $[e_0, e_f]$ . ♣

## References

- [1] Acikmese, B. and Ploen, S. R., “Convex Programming Approach to Powered Descent Guidance for Mars Landing,” *Journal of Guidance, Control and Dynamics*, Vol. 30, No. 5, 2007, pp. 1353–1366. [doi:10.2514/1.27553](https://doi.org/10.2514/1.27553).
- [2] Blackmore, L., Acikmese, B., and Scharf, D. P., “Minimum Landing Error Powered Descent Guidance for Mars Landing Using Convex Optimization,” *Journal of Guidance, Control and Dynamics*, Vol. 33, No. 4, 2010, pp. 1161–1171. [doi:10.2514/1.47202](https://doi.org/10.2514/1.47202).
- [3] Acikmese, B. and Blackmore, L., “Lossless Convexification for a Class of Optimal Problems with Nonconvex Control Constraints,” *Automatica*, Vol. 47, No. 2, 2011, pp. 341–347. [doi:10.1016/j.automatica.2010.10.037](https://doi.org/10.1016/j.automatica.2010.10.037).
- [4] Acikmese, B., Carson, J., and Blackmore, L., “Lossless Convexification of Nonconvex Control Bound and Pointing Constraints of the Soft Landing Optimal Control Problem,” *IEEE Transactions on Control Systems Technology*, Vol. 21, No. 6, 2013, pp. 2104–2113. [doi:10.1109/TCST.2012.2237346](https://doi.org/10.1109/TCST.2012.2237346).

- [5] Harris, M. W. and Acikmese, B., “Maximum Divert for Planetary Landing Using Convex Optimization,” *Journal of Optimization Theory and Applications*, Vol. 162, No. 3, 2013, pp. 975–995.  
[doi:10.1007/s10957-013-0501-7](https://doi.org/10.1007/s10957-013-0501-7).
- [6] Lu, P. and Liu, X., “Autonomous Trajectory Planning for Rendezvous and Proximity Operations by Conic Optimization,” *Journal of Guidance, Control, and Dynamics*, Vol. 36, No. 2, 2013, pp. 375–389.  
[doi:10.2514/1.58436](https://doi.org/10.2514/1.58436).
- [7] Liu, X. and Lu, P., “Solving Nonconvex Optimal Control Problems by Convex Optimization,” *Journal of Guidance, Control, and Dynamics*, Vol. 37, No. 3, 2014, pp. 750–765.  
[doi:10.2514/1.62110](https://doi.org/10.2514/1.62110).
- [8] Liu, X. and Lu, P., “Robust Trajectory Optimization for Highly Constrained Rendezvous and Proximity Operations,” AIAA Paper 2013-4720, Aug. 2013.  
[doi:10.2514/6.2013-4720](https://doi.org/10.2514/6.2013-4720).
- [9] Liu, X., *Autonomous Trajectory Planning by Convex Optimization*, Ph.D. thesis, Iowa State University, 2013, <http://lib.dr.iastate.edu/etd/13137>.
- [10] Harris, M. W. and Acikmese, B., “Minimum Time Rendezvous of Multiple Spacecraft Using Differential Drag,” *Journal of Guidance, Control and Dynamics*, Vol. 37, No. 2, 2014, pp. 365–373.  
[doi:10.2514/1.61505](https://doi.org/10.2514/1.61505).
- [11] Morgan, D., Chung, S.-J., and Hadaegh, F. Y., “Model Predictive Control of Swarms of Spacecraft Using Sequential Convex Optimization,” *Journal of Guidance, Control and Dynamics*, Vol. 37, No. 6, 2014, pp. 1725–1740.  
[doi:10.2514/1.G000218](https://doi.org/10.2514/1.G000218).
- [12] Boyd, S. and Vandenberghe, L., *Convex Optimization*, Cambridge University Press, New York, 2004, pp. 156–160 and 226.
- [13] Lobo, M. S., Vandenberghe, L., Boyd, S., and Lebret, H., “Applications of Second-Order Cone Programming,” *Linear Algebra and its Applications*, Vol. 284, 1998, pp. 193–228.  
[doi:10.1016/S0024-3795\(98\)10032-0](https://doi.org/10.1016/S0024-3795(98)10032-0).
- [14] Alizadeh, F. and Goldfarb, D., “Second-Order Cone Programming,” *Mathematical Programming*, Vol. 95, No. 1, 2003, pp. 3–51.  
[doi:10.1007/s10107-002-0339-5](https://doi.org/10.1007/s10107-002-0339-5).
- [15] Nesterov, Y. and Nemirovski, A., *Interior-Point Polynomial Algorithms in Convex Programming*, chap. 4, SIAM, Philadelphia, 1994.
- [16] Nesterov, Y. E. and Todd, M. J., “Self-Scaled Barriers and Interior-Point Methods for Convex Programming,” *Mathematics of Operations Research*, Vol. 22, No. 1, 1997, pp. 1–42.  
[doi:10.1287/moor.22.1.1](https://doi.org/10.1287/moor.22.1.1).
- [17] Sturm, J. F., “Implementation of Interior Point Methods for Mixed Semidefinite and Second Order Cone Optimization Problems,” *Optimization Methods and Software*, Vol. 17, No. 6, 2002, pp. 1105–1154.  
[doi:10.1080/1055678021000045123](https://doi.org/10.1080/1055678021000045123).

- [18] Andersen, E. D., Roos, C., and Terlaky, T., "On Implementing a Primal-Dual Interior-Point Method for Conic Quadratic Optimization," *Mathematical Programming*, Vol. 95, No. 2, 2003, pp. 249–277.  
[doi:10.1007/s10107-002-0349-3](https://doi.org/10.1007/s10107-002-0349-3).
- [19] Acikmese, B., Aung, M., Casoliva, J., Mohan, S., Johnson, A., Scharf, D., Masten, D., Scotkin, J., Wolf, A., and Regehr, M., "Flight Testing of Trajectories Computed by G-FOLD: Fuel Optimal Large Divert Guidance Algorithm for Planetary Landing," *23rd AAS/AIAA Spaceflight Mechanics Meeting*, Kauai, USA, To appear 2013.
- [20] Verschuer, D., Demeulenaere, B., Swevers, J., and Diehl, M., "Time-Optimal Path Tracking for Robots: A Convex Optimization Approach," *IEEE Transactions on Automatic Control*, Vol. 54, No. 10, 2009, pp. 2318–2327.  
[doi:10.1109/TAC.2009.2028959](https://doi.org/10.1109/TAC.2009.2028959).
- [21] Park, J., Haan, J., and Park, F. C., "Convex Optimization Algorithms for Active Balancing of Humanoid Robots," *IEEE Transactions on Robotics*, Vol. 23, No. 4, 2007, pp. 817–822.  
[doi:10.1109/TRO.2007.900639](https://doi.org/10.1109/TRO.2007.900639).
- [22] Josselyn, S. and Ross, I. M., "Rapid Verification Method for the Trajectory Optimization of Reentry Vehicles," *Journal of Guidance, Control and Dynamics*, Vol. 26, No. 3, 2003, pp. 505–508.  
[doi:10.2514/2.5074](https://doi.org/10.2514/2.5074).
- [23] Bollino, K. P., *High-Fidelity Real-Time Trajectory Optimization for Reusable Launch Vehicles*, Ph.D. thesis, Naval Postgraduate School, Monterey, CA, December 2006.
- [24] Shaffer, P. J., Ross, I. M., Oppenheimer, M. W., Doman, D. B., and Bollino, K. B., "Fault-Tolerant Optimal Trajectory Generation for Reusable Launch Vehicles," *Journal of Guidance, Control and Dynamics*, Vol. 30, No. 6, 2007, pp. 1794–1802.  
[doi:10.2514/1.27699](https://doi.org/10.2514/1.27699).
- [25] Jorris, T. R. and Cobb, R. G., "Multiple Method 2-D Trajectory Optimization Satisfying Waypoints and No-Fly Zone Constraints," *Journal of Guidance, Control and Dynamics*, Vol. 31, No. 3, 2008, pp. 543–553.  
[doi:10.2514/1.32354](https://doi.org/10.2514/1.32354).
- [26] Jorris, T. R. and Cobb, R. G., "Three-Dimensional Trajectory Optimization Satisfying Waypoint and No-Fly Zone Constraints," *Journal of Guidance, Control and Dynamics*, Vol. 32, No. 2, 2009, pp. 551–572.  
[doi:10.2514/1.37030](https://doi.org/10.2514/1.37030).
- [27] Schierman, J. D. and Hull, J. R., "In-Flight Entry Trajectory Optimization for Reusable Launch Vehicles," AIAA 2005-6434, Aug. 2005.  
[doi:10.2514/6.2005-6434](https://doi.org/10.2514/6.2005-6434).
- [28] Harpold, J. C. and Graves, C. A., "Shuttle Entry Guidance," *Journal of Astronautical Sciences*, Vol. 27, No. 3, 1979, pp. 239–268.
- [29] Lu, P., "Entry Guidance and Trajectory Control for Reusable Launch Vehicle," *Journal of Guidance, Control and Dynamics*, Vol. 20, No. 1, 1997, pp. 143–149.  
[doi:10.2514/2.4008](https://doi.org/10.2514/2.4008).

- [30] Betts, J. T., *Practical Methods for Optimal Control and Estimation Using Nonlinear Programming*, SIAM, Philadelphia, PA, 2nd ed., 2010, pp. 247–255.
- [31] Carson, J. M. and Acikmese, B., “A Model Predictive Control Technique with Guaranteed Resolvability and Required Thruster,” AIAA Paper 2006-6780, Aug., 2006.
- [32] Lu, P., “Entry Guidance: A Unified Method,” *Journal of Guidance, Control, and Dynamics*, Vol. 37, No. 3, 2014, pp. 713–728.  
[doi:10.2514/1.62605](https://doi.org/10.2514/1.62605).
- [33] Shaffer, P. J., *Optimal Trajectory Reconfiguration and Retargeting for the X-33 Reusable Launch Vehicle*, Master’s thesis, Naval Postgraduate School, Monterey, CA, 2004.
- [34] Lu, P., Cerimele, C., Tigges, M., and Matz, D., “Optimal Aerocapture Guidance,” *Journal of Guidance, Control, and Dynamics*, accepted for publication 2014.  
[doi:10.2514/1.G000713](https://doi.org/10.2514/1.G000713).
- [35] Morozov, V. A., *Regularization Methods for Ill-Posed Problems*, CRC Press, Boca Raton, FL, 2nd ed., 1993, pp. 192–209.
- [36] Harris, M. W. and Acikmese, B., “Lossless Convexification of Non-convex Optimal Control Problems for State Constrained Linear Systems,” *Automatica*, Vol. 50, No. 9, 2014, pp. 2304–2311.  
[doi:10.1016/j.automatica.2014.06.008](https://doi.org/10.1016/j.automatica.2014.06.008).
- [37] Shen, Z. and Lu, P., “Onboard Generation of Three-Dimensional Constrained Entry Trajectories,” *Journal of Guidance, Control, and Dynamics*, Vol. 26, No. 1, 2003, pp. 111–121.  
[doi:10.2514/2.5021](https://doi.org/10.2514/2.5021).
- [38] Phillips, T. H., “A Common Aero Vehicle (CAV) Model, Description, and Employment Guide,” Schafer Corp. for Air Force Research Laboratory and Air Force Space Command, Jan. 2003.
- [39] Löfberg, J., “YALMIP: A Toolbox for Modeling and Optimization in MATLAB,” in Proceedings of the CACSD conference, Taipei, Taiwan, 2004, pp. 284–289.  
[doi:10.1109/CACSD.2004.1393890](https://doi.org/10.1109/CACSD.2004.1393890).
- [40] Becerra, V., “PSOPT Optimal Control Solver User Manual. Release 3,” Available: <http://code.google.com/p/psopt/downloads/list>, [retrieved 14 February 2015].
- [41] Wachter, A. and Biegler, L. T., “On the Implementation of a Primal-Dual Interior Point Filter Line Search Algorithm for Large-Scale Nonlinear Programming,” *Mathematical Programming*, Vol. 106, No. 1, 2006, pp. 25–57.  
[doi:10.1007/s10107-004-0559-y](https://doi.org/10.1007/s10107-004-0559-y).
- [42] Domahidi, A., Chu, E., and Boyd, S., “ECOS: an SOCP Solver for Embedded System,” European Control Conference, Zurich, Switzerland, 2013, pp. 3071–3076.
- [43] Hartl, R., Sethi, S., and Vickson, R., “A Survey of the Maximum Principles for Optimal Control Problems with State Constraints,” *SIAM Review*, Vol. 37, No. 2, 1995, pp. 181–218.  
[doi:10.1137/1037043](https://doi.org/10.1137/1037043).